HERMES impact for the access of Compton form factors

K. Kumerički[a], D. Müller[b], and M. Murray[c]

[a] *Department of Physics, University of Zagreb*
HR-10002 Zagreb, Croatia

[b]*Institut für Theoretische Physik II, Ruhr-Universität Bochum*
D-44780 Bochum, Germany

[c] *School of Physics and Astronomy, University of Glasgow*
G128QQ Glasgow, Scotland, UK

Abstract

We utilize the DVCS asymmetry measurements of the HERMES collaboration for access to Compton form factors in the deeply virtual regime and to generalized parton distributions. In particular, the (almost) complete measurement of DVCS observables allows us to map various asymmetries into the space of Compton form factors, where we still rely in this analysis on dominance of twist-two associated Compton form factors. We compare this one-to-one map with local Compton form factor fits and a model dependent global fit.

arXiv:1301.1230v1 [hep-ph] 7 Jan 2013

Contents

1 Introduction

As is well known, at the beginning of the last century Compton scattering played a crucial role in the debate on the dual nature of light. Namely, if light scatters off an electron, energy is transferred to the electron and so the wavelength of the scattered light increases. In addition to this Compton effect revealing the particle aspect of light [1], the Compton scattering process has now many applications in material science, medicine, astro- and particle physics, where in particular, it is utilized to probe the electron wave function in matter. In hadronic physics the Compton scattering process is used to reveal static properties of the nucleon in terms of electric and magnetic polarizabilities. Its generalization into virtual Compton scattering [2] offers a supplementing window to electromagnetic form factor studies, which have been intensively performed in the last six decades. At larger photon virtualities $\mathcal{Q}^2 \gtrsim 1\text{GeV}^2$, the Compton scattering process probes the partonic content of the nucleon and gives access to the so-called generalized parton distributions (GPDs) [3, 4, 5]. In particular, it was suggested to measure by means of deeply virtual Compton scattering (DVCS) the quark orbital angular momentum [6] and to access the transverse distributions of partons [7, 8]. With these goals in mind, many experimental and theoretical activities were started in the field of hard exclusive processes, where we consider the measurements of (DV)CS observables as important as the measurements of electromagnetic form factors.

Measurements of DVCS have taken place at HERA and Jefferson Lab since the turn of the millennium, with the aim of understanding the decomposition of the nucleon spin. The first observed DVCS candidate events at high energy were announced by the ZEUS collaboration using a collider experiment at HERA in 2000 [9] and few months later for fixed target kinematics [10]. The first DVCS measurements in fixed target experiments were published simultaneously by the HERMES and CLAS collaborations a year later [11, 12]. Both experiments measured the beam spin asymmetry arising from the interference term between DVCS and elastic scattering with bremsstrahlung in the scattering amplitude. The latter process, called the Bethe-Heitler (BH) process, has the same initial and final states as DVCS ($ep \rightarrow ep\gamma$) and at fixed target kinematics typically the interference term in the scattering amplitude is more experimentally accessible than the pure DVCS term [13]. Both HERMES and CLAS utilized the fact that the large BH contribution in the interference term at $\mathcal{Q}^2 \sim 2\,\text{GeV}^2$ and $-t \sim 0.1\,\text{GeV}^2$ amplifies the contribution from the more interesting DVCS process.

Since then, large experimental effort has been expended to measure various observables in the electroproduction of photons and mesons. The phenomenological challenge is now to describe these data in terms of GPDs, which requires a flexible model. Thereby, we meet a more elementary problem, in particular for DVCS: the number of Compton form factors (or helicity

amplitudes) is usually larger than the number of observables at a given kinematical point. One must therefore rely on model assumptions or hypotheses which means that, independently of the applied method or framework, a theoretical bias cannot be avoided in analyzing the present available world data set. This may even lead to a qualitative misinterpretation of the data, where the apparent influence of any particular GPD model set may be determined more by the initial theoretical approach to the problem than by the observed data.

In this paper we will concentrate on the results from the HERMES collaboration, which had both electron and positron beams available and is currently the experiment that has delivered the most complete set of DVCS observables. In Sect. 2 we introduce the DVCS observables and we give details on the HERMES experiment. In Sect. 3 we consider the extraction of CFFs at given kinematical points from the HERMES measurements as a map of random variables. Additionally, we utilise the regression approach and use the HERMES data to access CFFs by least squares fitting. We also present a global GPD model fit that additionally includes HERA collider and Jefferson Lab measurements and conclude on what we have learned. Finally, we summarize and provide an outlook.

2 HERMES measurements of DVCS observables

2.1 Definitions of photon leptoproduction observables

The DVCS process enters as a subprocess in deeply virtual photon leptoproduction and its amplitude can be decomposed in terms of twelve independent helicity amplitudes given in some reference frame. Alternatively, we might parameterize the DVCS amplitude in Lorentz-invariant Compton form factors (CFFs), which are defined in analogy to GPD definitions and are called [14]:

$$\mathcal{F} \in \left\{ \mathcal{H}, \mathcal{E}, \widetilde{\mathcal{H}}, \widetilde{\mathcal{E}} \right\} , \quad \mathcal{F}_{\text{eff}} \in \left\{ \mathcal{H}_{\text{eff}}, \mathcal{E}_{\text{eff}}, \widetilde{\mathcal{H}}_{\text{eff}}, \widetilde{\mathcal{E}}_{\text{eff}} \right\} , \quad \mathcal{F}_{\text{T}} \in \left\{ \mathcal{H}_{\text{T}}, \mathcal{E}_{\text{T}}, \widetilde{\mathcal{H}}_{\text{T}}, \widetilde{\mathcal{E}}_{\text{T}} \right\} , \quad (1)$$

where we separated them into twist-two related CFFs $\mathcal{F}$, twist-three related CFFs $\mathcal{F}_{\text{eff}}$, and transversity CFFs $\mathcal{F}_{\text{T}}$. Unfortunately, different conventions, which differ by power suppressed contributions, are used in the literature. As noted previously, the DVCS subprocess is accompanied by the Bethe-Heitler bremsstrahlung process, the amplitude of which is, at leading order in the QED fine structure constant, real-valued. Moreover, it is entirely parameterized in terms of the electromagnetic form factors, which for the nucleon are well-known for the kinematics of interest. The interference term of both subprocesses is charge-odd and depends linearly on the CFFs, while, the BH-squared, depending only on electromagnetic form factors, and DVCS-squared, given as bilinear form of CFFs, amplitudes are charge-even. The differential cross
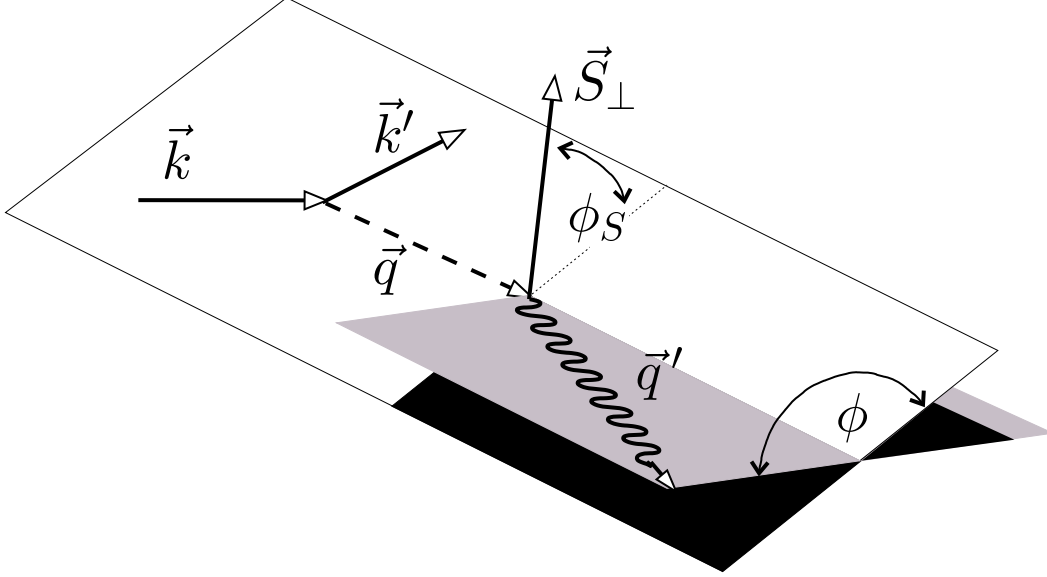
Figure 1: Reference frame adopted by the HERMES collaboration [15].

section, for the most general setup, is five-fold and we write it in terms of the Bjorken scaling variable x_{B}, the negative virtuality squared of the intermediate photon $\mathcal{Q}^2 = -q^2$, the momentum transfer square in the t-channel, and two relative azimuthal angles ϕ, between lepton scattering plane and reaction plane, and φ, between lepton scattering plane and transverse spin polarization vector, as in [14]:

$$\frac{d^5\sigma}{dx_{\mathrm{B}}d\mathcal{Q}^2dtd\phi d\varphi} = \frac{\alpha^3 x_{\mathrm{B}} y^2}{16\pi^2 \mathcal{Q}^4 \sqrt{1 + \frac{4x_{\mathrm{B}}^2 M_p^2}{\mathcal{Q}^2}}} \left[\frac{|\mathcal{T}_{\mathrm{BH}}|^2}{e^6} + \frac{\mathcal{I}(\mathcal{F})}{e^6} + \frac{|\mathcal{T}_{\mathrm{DVCS}}|^2(\mathcal{F}^*, \mathcal{F})}{e^6} \right] (x_{\mathrm{B}}, \mathcal{Q}^2, t, \phi, \varphi) , \tag{2}$$

where $\alpha = e^2/4\pi$ is the electromagnetic fine structure constant and M_p is the proton mass. Here, and in the following, we neglect the electron mass and define the azimuthal angle in an reference frame where the photon travels along the z-axis and the x-component of the incoming electron is positive, see Fig. 1. This frame has been adopted by the HERMES collaboration. Compared to the BMK conventions in [14], in which the photon travels in opposite direction of the z-axis, for the frame used by HERMES we have the relations

$$\phi^{\mathrm{BMK}} \equiv \phi_N^{\mathrm{BMK}} - \phi_e^{\mathrm{BMK}} = \pi - \phi , \qquad \phi \equiv \phi_\gamma - \phi_e \tag{3}$$

$$\varphi^{\mathrm{BMK}} \equiv \Phi^{\mathrm{BMK}} - \phi_N^{\mathrm{BMK}} = \varphi - \pi , \qquad \varphi = \phi_\gamma - \phi_{\mathrm{S}} , \tag{4}$$

where ϕ_N, $\phi_\gamma = \phi_N + \pi$, $\phi_e = 0$, and $\Phi \equiv \phi_{\mathrm{S}}$ are the azimuthal angles of the nucleon, photon, electron, and the transverse polarization vector, respectively.

4

The Fourier expansion of the various amplitude squares may be written in analogy to the notation of [14] as

$$|\mathcal{T}_{\mathrm{BH}}|^2 = \frac{e^6}{-t\,x_{\mathrm{B}}^2\,w(\phi)} \left\{ \hat{c}_0^{\mathrm{BH}} + \sum_{n=1}^{2} \hat{c}_n^{\mathrm{BH}} \cos(n\phi) + \hat{s}_1^{\mathrm{BH}} \sin\phi \right\}, \tag{5}$$

$$\mathcal{I} = \frac{\pm e^6}{-t\,x_{\mathrm{B}}^2\,w(\phi)} \left\{ \hat{c}_0^{\mathcal{I}} + \sum_{n=1}^{3} \left[\hat{c}_n^{\mathcal{I}} \cos(n\phi) + \hat{s}_n^{\mathcal{I}} \sin(n\phi) \right] \right\}, \tag{6}$$

$$|\mathcal{T}_{\mathrm{DVCS}}|^2 = \frac{e^6}{y^2\,\mathcal{Q}^2\,x_{\mathrm{B}}^2} \left\{ \hat{c}_0^{\mathrm{DVCS}} + \sum_{n=1}^{2} \left[\hat{c}_n^{\mathrm{DVCS}} \cos(n\phi) + \hat{s}_n^{\mathrm{DVCS}} \right] \right\}. \tag{7}$$

Here, the $+$ $(-)$ overall sign of the interference term (6) refers to an electron (positron) beam, $1/w(\phi) \propto 1/\mathcal{P}_1(\phi)\mathcal{P}_2(\phi)$ is the product of scaled BH propagators given in [14], which is expanded in the even harmonics of ϕ up the second order,

$$w(\phi) = 1 + w_1 \cos(\phi) + w_2 \cos(2\phi). \tag{8}$$

Note that we included a generic kinematical overall factor $\sqrt{-t/(y^2\mathcal{Q}^2)}$ from the interference term (6) in the definition of the Fourier coefficients. Moreover, if the differential cross section (2) is weighted with $w(\phi)$, its Fourier expansion w.r.t. the azimuthal angles becomes finite.

Having both electrons and positrons with which to make measurements, one can access the interference and DVCS-squared terms by means of cross section differences and sums

$$d\sigma_I(\phi,\varphi) \stackrel{\mathrm{LO_{QED}}}{\equiv} d\sigma_{\mathrm{odd}}(\phi,\varphi) = \frac{1}{2}\left[d\sigma_+ - d\sigma_-\right](\phi,\varphi), \quad d\sigma_{\mathrm{even}}(\phi,\varphi) = \frac{1}{2}\left[d\sigma_+ + d\sigma_-\right](\phi,\varphi). \tag{9}$$

Measuring such charge-odd cross sections with different lepton and nucleon polarizations, one can, in principle, reach an almost complete decomposition in terms of the twelve CFFs (1). Namely, in the deeply virtual regime, the first and second order harmonics of the weighted differential cross section differences are dominated by linear combinations of twist-two and twist-three related CFFs $\mathcal{F}$ and $\mathcal{F}_{\mathrm{eff}}$ respectively, while the third harmonic is related to the transversity CFFs $\mathcal{F}_{\mathrm{T}}$. In the first two cases the number of possible observables allows access to both the imaginary and real parts of the corresponding form factors, while in the latter case only one combination of $\mathfrak{Re}\,\mathcal{F}_{\mathrm{T}}$ and three combinations of $\mathfrak{Im}\,\mathcal{F}_{\mathrm{T}}$ can be accessed. Moreover, in this approximation the constant terms are governed only by twist-two associated CFFs $\mathcal{F}$ and, hence, such measurements allow for an experimental consistency check of the underlying formalism, given in some approximation.

The charge-even combination may serve also for an experimental consistency check or may be used to access the desired CFFs in a different manner. Most importantly, in single spin-flip experiments, the BH term drops out in the considered order of QED and so such measurements

give direct access to bilinear CFF combinations. In double spin-flip experiments one needs to subtract the BH-squared term, which may be feasible at small x_B where an effective 'pomeron' behavior may overwhelm the contributions of the BH subprocess.

Thus far, only HERA experiments at DESY had both charges of lepton beams at hand. The HERMES experiment achieved measurements with polarized electron and positron beams for longitudinal and transversal target spin polarizations and thus the following asymmetries where extracted.

- Single beam-spin asymmetries in the charge-odd and charge-even sectors:

$$A_\text{LU,I}(\phi) = \frac{\left[d\sigma_+^\rightarrow - d\sigma_+^\leftarrow\right] - \left[d\sigma_-^\rightarrow - d\sigma_-^\leftarrow\right]}{d\sigma_+^\rightarrow + d\sigma_+^\leftarrow + d\sigma_-^\rightarrow + d\sigma_-^\leftarrow} , \tag{10}$$

$$A_\text{LU,DVCS}(\phi) = \frac{\left[d\sigma_+^\rightarrow - d\sigma_+^\leftarrow\right] + \left[d\sigma_-^\rightarrow - d\sigma_-^\leftarrow\right]}{d\sigma_+^\rightarrow + d\sigma_+^\leftarrow + d\sigma_-^\rightarrow + d\sigma_-^\leftarrow} , \tag{11}$$

where $\rightarrow$ ($\leftarrow$) denotes electron ($-$) or positron ($+$) polarization along (opposite to) the beam direction.

- Beam-charge asymmetry:

$$A_\text{C}(\phi) = \frac{d\sigma_+ - d\sigma_-}{d\sigma_+ + d\sigma_-} . \tag{12}$$

- Single and double longitudinal target-spin asymmetries with a positron beam:

$$A_\text{UL,+}(\phi) = \frac{d\sigma_+^\Leftarrow - d\sigma_+^\Rightarrow}{d\sigma_+^\Leftarrow + d\sigma_+^\Rightarrow} , \tag{13}$$

$$A_\text{LL,+}(\phi) = \frac{\left[d\sigma_+^{\leftarrow\Rightarrow} + d\sigma_+^{\rightarrow\Leftarrow}\right] - \left[d\sigma_+^{\rightarrow\Rightarrow} + d\sigma_+^{\leftarrow\Leftarrow}\right]}{d\sigma_+^{\leftarrow\Rightarrow} + d\sigma_+^{\rightarrow\Leftarrow} + d\sigma_+^{\rightarrow\Rightarrow} + d\sigma_+^{\leftarrow\Leftarrow}} . \tag{14}$$

Note that, contrary to HERMES notation, $\Leftarrow$ ($\Rightarrow$) denotes proton polarization opposite to (along) the positron beam direction.

- Single transverse target-spin asymmetries in the charge-odd and charge-even sectors:

$$A_\text{UT,I}(\phi, \varphi) = \frac{\left[d\sigma_+^\Uparrow - d\sigma_+^\Downarrow\right] - \left[d\sigma_-^\Uparrow - d\sigma_-^\Downarrow\right]}{d\sigma_+^\Uparrow + d\sigma_+^\Downarrow + d\sigma_-^\Uparrow + d\sigma_-^\Downarrow} , \tag{15}$$

$$A_\text{UT,DVCS}(\phi, \varphi) = \frac{\left[d\sigma_+^\Uparrow - d\sigma_+^\Downarrow\right] + \left[d\sigma_-^\Uparrow - d\sigma_-^\Downarrow\right]}{d\sigma_+^\Uparrow + d\sigma_+^\Downarrow + d\sigma_-^\Uparrow + d\sigma_-^\Downarrow} . \tag{16}$$

- Double longitudinal beam and transverse target-spin asymmetries in the charge-odd and charge-even sectors:

$$A_{\mathrm{LT,I}}(\phi,\varphi) = \frac{\left[d\sigma_+^{\rightarrow\Uparrow} + d\sigma_+^{\leftarrow\Downarrow}\right] - \left[d\sigma_+^{\rightarrow\Downarrow} + d\sigma_+^{\leftarrow\Uparrow}\right] - \left[d\sigma_-^{\rightarrow\Uparrow} + d\sigma_-^{\leftarrow\Downarrow}\right] + \left[d\sigma_-^{\rightarrow\Downarrow} + d\sigma_-^{\leftarrow\Uparrow}\right]}{d\sigma_+^{\rightarrow\Uparrow} + d\sigma_+^{\leftarrow\Downarrow} + d\sigma_+^{\rightarrow\Downarrow} + d\sigma_+^{\leftarrow\Uparrow} + d\sigma_-^{\leftarrow\Downarrow} + d\sigma_-^{\rightarrow\Uparrow} + d\sigma_-^{\rightarrow\Downarrow} + d\sigma_-^{\leftarrow\Uparrow}},$$

(17)

$$A_{\mathrm{LT,even}}(\phi,\varphi) = \frac{\left[d\sigma_+^{\rightarrow\Uparrow} + d\sigma_+^{\leftarrow\Downarrow}\right] - \left[d\sigma_+^{\rightarrow\Downarrow} + d\sigma_+^{\leftarrow\Uparrow}\right] + \left[d\sigma_-^{\rightarrow\Uparrow} + d\sigma_-^{\leftarrow\Downarrow}\right] - \left[d\sigma_-^{\rightarrow\Downarrow} + d\sigma_-^{\leftarrow\Uparrow}\right]}{d\sigma_+^{\rightarrow\Uparrow} + d\sigma_+^{\leftarrow\Downarrow} + d\sigma_+^{\rightarrow\Downarrow} + d\sigma_+^{\leftarrow\Uparrow} + d\sigma_-^{\leftarrow\Downarrow} + d\sigma_-^{\rightarrow\Uparrow} + d\sigma_-^{\rightarrow\Downarrow} + d\sigma_-^{\leftarrow\Uparrow}}.$$

(18)

All these observables can be theoretically expressed in terms of weighted cross sections. However, since the denominator given by the unpolarized cross section depends on the azimuthal angle ϕ, they are given by a series of ϕ harmonics rather than finite sums. Nevertheless, in the kinematics where the BH process dominates, the zeroth and first harmonics of these asymmetries are roughly determined by the linear combinations of twist-two associated CFFs $\mathcal{F}$ that enter the interference term. Note also that, except for the longitudinal target spin asymmetries (13) and (14), the denominators are expressed by the charge-even cross section. Utilizing the charge asymmetry (12), we find in general that an asymmetry measured with a positron (or electron) beam can be expressed by charge-odd (interference term) and charge-even (a possible squared BH term plus a DVCS-squared term) expression:

$$A_{\cdots,+}(\phi) = \frac{A_{\cdots,\mathrm{I}}(\phi)}{1 + A_{\mathrm{C}}(\phi)} + \frac{A_{\cdots,\mathrm{BH}}(\phi) + A_{\cdots,\mathrm{DVCS}}(\phi)}{1 + A_{\mathrm{C}}(\phi)}.$$

(19)

Assuming that the BH amplitude overwhelms the DVCS one, we may drop the DVCS induced part and we approximately have

$$A_{\cdots,\mathrm{I}}(\phi) \approx A_{\cdots,+}(\phi)\left[1 + A_{\mathrm{C}}(\phi)\right] - A_{\cdots,\mathrm{BH}}(\phi),$$

(20)

where the BH-associated asymmetry $A_{\cdots,\mathrm{BH}}(\phi)$ drops out in single-spin asymmetries. We add that the double-spin asymmetry in the charge-odd sector is defined in terms of cross sections as

$$A_{\mathrm{LL,I}}(\phi) = \frac{\left[d\sigma_+^{\rightarrow\Rightarrow} + d\sigma_+^{\leftarrow\Leftarrow}\right] - \left[d\sigma_+^{\leftarrow\Rightarrow} + d\sigma_+^{\rightarrow\Leftarrow}\right] - \left[d\sigma_-^{\rightarrow\Rightarrow} + d\sigma_-^{\leftarrow\Leftarrow}\right] + \left[d\sigma_-^{\leftarrow\Rightarrow} + d\sigma_-^{\rightarrow\Leftarrow}\right]}{d\sigma_+^{\rightarrow\Rightarrow} + d\sigma_+^{\leftarrow\Leftarrow} + d\sigma_+^{\leftarrow\Rightarrow} + d\sigma_+^{\rightarrow\Leftarrow} + d\sigma_-^{\rightarrow\Rightarrow} + d\sigma_-^{\leftarrow\Leftarrow} + d\sigma_-^{\leftarrow\Rightarrow} + d\sigma_-^{\rightarrow\Leftarrow}}.$$

(21)

Let us finally remind the reader here that asymmetries are expanded in an infinite Fourier series. Hence, the method for the extraction of CFFs, outlined above for cross section differences, has to be modified. For illustration let us consider here the lepton beam-spin (10) and beam-charge (12) asymmetries that offer access to the imaginary and real parts of CFFs respectively.

7

Substituting the cross section (2) and the harmonic expansions (5,6,7) into (10) and (12), we find the azimuthal angle dependencies of the charge-odd electron beam spin and charge asymmetry respectively:

$$A_{\mathrm{LU,I}}(\phi) = \frac{\hat{s}_1^{\mathcal{I}} \sin(\phi) + \hat{s}_2^{\mathcal{I}} \sin(2\phi)}{\sum_{n=0}^{2} \hat{c}_n^{\mathrm{BH}} \cos(n\phi) + \frac{-t}{y^2 \mathcal{Q}^2} w(\phi) \sum_{n=0}^{2} \hat{c}_n^{\mathrm{DVCS}} \cos(n\phi)}, \tag{22}$$

$$A_{\mathrm{C}}(\phi) = \frac{\hat{c}_0^{\mathcal{I}} + \hat{c}_1^{\mathcal{I}} \cos(\phi) + \hat{c}_2^{\mathcal{I}} \cos(2\phi) + \hat{c}_3^{\mathcal{I}} \cos(3\phi)}{\sum_{n=0}^{2} \hat{c}_n^{\mathrm{BH}} \cos(n\phi) + \frac{-t}{y^2 \mathcal{Q}^2} w(\phi) \sum_{n=0}^{2} \hat{c}_n^{\mathrm{DVCS}} \cos(n\phi)}, \tag{23}$$

where the odd and even Fourier coefficients $\hat{s}_n^{\mathcal{I}}$ and $\hat{c}_n^{\mathcal{I}}$ of the interference term are linear functions of the imaginary and real parts of the CFFs and the even DVCS Fourier coefficients $\hat{c}_n^{\mathrm{DVCS}}$ are bilinear in all CFFs. In the $1/\mathcal{Q}$ expansion, the first harmonics of the interference term dominate and are governed by the CFFs $\mathcal{F}$, the second harmonics are relatively suppressed by $\sqrt{(t_{\min} - t)/\mathcal{Q}^2}$ and determined by the CFF $\mathcal{F}_{\mathrm{eff}}$ while the third harmonic of the charge asymmetry (23) is given by the CFFs $\mathcal{F}_{\mathrm{T}}$ and, to leading-twist accuracy, is predicted by the gluon transversity GPD. In reality, however, all harmonics of the interference term are functions of all twelve CFFs [16, 17]. Note that the third odd harmonic is absent and hence the imaginary part of the transversity CFF combination cannot be accessed from the interference term. In principle, this missing information is contained in the DVCS-squared term. Besides the mixing of the various CFFs for a given harmonic, the projection

$$A_{\mathrm{LU,I}}^{\sin(n\phi)} = \frac{1}{\pi} \int_{-\pi}^{\pi} d\phi \, \sin(n\phi) A_{\mathrm{LU,I}}(\phi) \,, \tag{24}$$

$$A_{\mathrm{C}}^{\cos(n\phi)} = \frac{1}{\pi} \int_{-\pi}^{\pi} d\phi \, \cos(n\phi) A_{\mathrm{C}}(\phi) \ \text{ for } \ n > 0 \,, \qquad A_{\mathrm{C}}^{\cos(0\phi)} = \frac{1}{2\pi} \int_{-\pi}^{\pi} d\phi \, A_{\mathrm{C}}(\phi) \,, \tag{25}$$

yields an additional contamination due to the ϕ dependence in the denominator.

2.2 Experimental details

Exclusive photon events at HERMES were selected if having exactly one photon and one lepton track detected within the acceptance of the spectrometer. The event selection was subject to the kinematic constraints

$$1 \, \mathrm{GeV}^2 < \mathcal{Q}^2 < 10 \, \mathrm{GeV}^2 \,, \ \ 0.03 < x_{\mathrm{B}} < 0.35 \,, \ \ -t < 0.7 \, \mathrm{GeV}^2 \,, \ \ W^2 > 9 \, \mathrm{GeV}^2 \,, \ \text{ and } \nu < 22 \, \mathrm{GeV} \,,$$

where W is the invariant mass of the $\gamma^* p$ system and ν is the energy of the virtual photon in the target rest frame. The polar angle between the directions of the virtual and real photons was required to be within the limits 5 mrad $< \theta_{\gamma^* \gamma} <$ 45 mrad.

An event sample was selected requiring that the squared missing-mass $M_{\mathrm{X}}^2 = (q + M_p - q')^2$ of the $e \, p \rightarrow e' \, \gamma \, \mathrm{X}$ measurement corresponded to the square of the proton mass, M_p, within the

bin no.	1	2	3	4	5	6	7	8	9	10	11	12
$-t$ [GeV^2]	0.03	0.1	0.2	0.42	0.1	0.1	0.13	0.2	0.08	0.1	0.13	0.19
x_B	0.08	0.1	0.11	0.12	0.05	0.08	0.12	0.2	0.06	0.08	0.11	0.17
$\mathcal{Q}^2$ [GeV^2]	1.9	2.5	2.9	3.5	1.5	2.2	3.1	5.0	1.2	1.9	2.8	4.9

Table 1: Kinematical values of three times four HERMES bins from ref. [13], labeled as #1, $\cdots$, #12.

limits of the energy resolution of the HERMES spectrometer (mainly the calorimeter). Recall that q is the four-momentum of the virtual photon, p is the initial four-momentum of the target proton and q' is the four-momentum of the produced photon. The "exclusive region" was defined as $-(1.5\,\mathrm{GeV})^2 < M_X^2 < (1.7\,\mathrm{GeV})^2$. This exclusive region was shifted by up to $0.17\,\mathrm{GeV}^2$ for certain subsets of the data in order to reflect observed differences in the distributions of the electron and positron data samples. A systematic uncertainty contribution is assigned for this effect. This event sample selection technique was used as it allows for the most complete set of DVCS observable measurements to be considered; although results using the measurement of the recoiling proton have been released by HERMES [18], this technique is only currently available for beam-spin DVCS measurements and was never utilised with a polarised target. Other systematic uncertainty contributions arise from potential misalignment of the spectrometer, acceptance and smearing effects, and the inclusion in the data set from misidentified semi-inclusive deep inelastic scattering events. The latter is mitigated somewhat using a correction procedure. The sizes of the systematic uncertainties are estimated using Monte Carlo techniques.

The data sample in the exclusive region contains events not only involving the production of real photons in which the proton remains intact, but also events involving the excitation of the target proton to a Δ^+ resonant state ("associated production"). This is a consequence of using a missing-mass event sample selection technique as noted above; the calorimeter resolution for measuring the produced photon does not allow separation of the resonant events from the rest of the data sample. No systematic uncertainty is assigned for the contribution from these events; they are treated as part of the signal. A Monte Carlo calculation based on the parameterisation from ref. [19] is used to estimate the fractional contribution to the event sample from resonant production in each kinematic bin; the uncertainty on this estimate cannot be adequately quantified because no sufficiently precise measurements have been made in the HERMES kinematic region. The results of the estimate, called the associated fractions and labelled "Assoc. fraction", are shown in refs. [13, 15, 20, 21, 22]. The method used to perform this estimation is described in detail in ref. [13].

The HERMES measurements were presented in terms of four or six bins times three one dimensional projection in $-t$, x_B, and $\mathcal{Q}^2$ (see Tab. 1). The projections in the kinematic variables
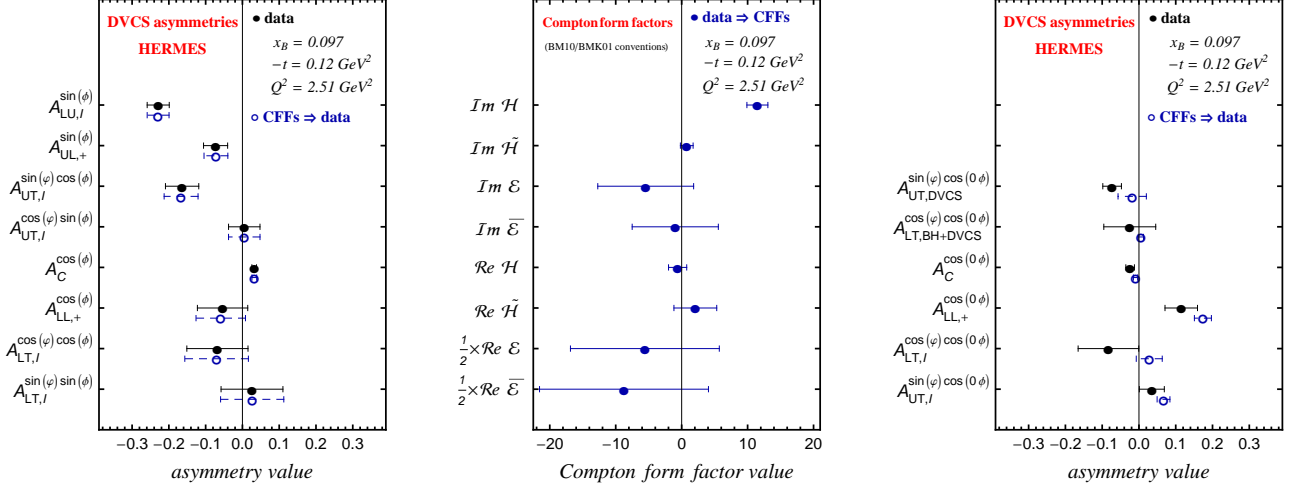
Figure 2: HERMES measurements (solid circles) of interference dominated asymmetries in the twist-two sector (left) and BH/DVCS-squared dominated as well as charge odd twist-tree asymmetries (right) at the overall mean values $x_B = 0.097$, $t = -0.119\,\text{GeV}^2$, and $\mathcal{Q}^2 = 2.51\,\text{GeV}^2$. In the middle panel the resulting CFFs from a linearized map of the interference dominated asymmetries are displayed. The empty circles, shown in the left and right panels, arise from the inverse linearized map of extracted CFFs back to asymmetries.

are each correlated; the $\mathcal{Q}^2$ and x_B projections are very highly correlated as a consequence of the experimental design. For our analyses we employ the four bin data, where the four-binned version of the six-binned data for the beam spin and charge asymmetries from the HERMES measurements, published in ref. [22], were provided to us by the HERMES collaboration. We neglect the small differences in the kinematical means of different asymmetry measurements, which are very much within the experimental uncertainty and take the values that are listed in Tab. 1, labeled as bin #1, $\cdots$, #12. Alternatively, we take the kinematical values that are given in the publications, assuming that the asymmetry values do not vary within the small changes in the mean kinematic values. The selected set of *fourteen* observables out of the *thirty-four* asymmetry measurements, which we will use, are shown in Fig. 2 as solid circles at the overall mean values $x_B = 0.097$, $t = -0.119\,\text{GeV}^2$, and $\mathcal{Q}^2 = 2.51\,\text{GeV}^2$.

3 Analysis of HERMES data

In Sect. 3.1 we first illustrate which information one may extract from the HERMES measurements, cf. Fig. 2, if one assumes that effective twist-three and transverse photon helicity flip effects are absent. Employing the BMK formulae set [14], we will also show that data are not in contradiction with this hypothesis. The outline of the remainder is as following: in Sect. 3.2 we

give a review of the methods used to analyze DVCS data and introduce the (non-)linear mapping method. In Sect. 3.3.1 this method is then applied to the HERMES data and in Sect. 3.3.2 we analyze the same data with local CFF fits. Finally, in Sect. 3.4 we present a global CFF fit with a simple GPD model used previously in global fits to DVCS data off unpolarized protons. Finally, we discuss the implications of our analyses for GPD model building.

3.1 Asymmetries in terms of CFFs

Relying on the dominance of the BH-squared term over the DVCS-squared term and approximating the BH-squared term by its dominant constant harmonic, the following linear combinations of CFFs enter in the various asymmetries (here we set the minimal value of $-t$ to zero):

- The first harmonics of single beam spin (10) and beam charge (12) asymmetries,

$$A_{\text{LU,I}}^{\sin(1\phi)} \propto -\frac{y\sqrt{1-y}}{2-2y+y^2}\sqrt{\frac{-t}{y^2 \mathcal{Q}^2}} \times x_{\text{B}} \, \mathfrak{Im}\left[\mathcal{C}_{\text{unp}}^{\text{I}}(\mathcal{F}) + \cdots\right], \tag{26}$$

$$A_{\text{C}}^{\cos(1\phi)} \propto -\frac{\sqrt{1-y}}{2-y}\sqrt{\frac{-t}{y^2 \mathcal{Q}^2}} \times x_{\text{B}} \, \mathfrak{Re}\left[\mathcal{C}_{\text{unp}}^{\text{I}}(\mathcal{F}) + \cdots\right], \tag{27}$$

are *approximately* given by the imaginary and real part of the linear combination

$$\mathcal{C}_{\text{unp}}^{\text{I}}(\mathcal{F}) \approx F_1 \mathcal{H} - \frac{t}{4M_p^2} F_2 \mathcal{E} + \frac{x_{\text{B}}}{2}(F_1 + F_2)\widetilde{\mathcal{H}}. \tag{28}$$

- The first harmonics of single longitudinal target spin asymmetry (13) and double longitudinal target spin asymmetry (14)

$$A_{\text{UL,+}}^{\sin(1\phi)} \propto -\frac{\sqrt{1-y}}{2-y}\sqrt{\frac{-t}{y^2 \mathcal{Q}^2}} \times x_{\text{B}} \, \mathfrak{Im}\left[\mathcal{C}_{\text{LP}}^{\text{I}}(\mathcal{F}) + \cdots\right] + \text{DVCS}^2\text{-term}, \tag{29}$$

$$A_{\text{LL,+}}^{\cos(1\phi)} \propto -\frac{y\sqrt{1-y}}{2-2y+y^2}\sqrt{\frac{-t}{y^2 \mathcal{Q}^2}} \times x_{\text{B}} \, \mathfrak{Re}\left[\mathcal{C}_{\text{LP}}^{\text{I}}(\mathcal{F}) + \cdots\right] + \text{BH}^2\text{-term} + \text{DVCS}^2\text{-term}, \tag{30}$$

are *approximately* governed by the imaginary and real part of the linear combination

$$\mathcal{C}_{\text{LP}}^{\text{I}}(\mathcal{F}) \approx F_1 \widetilde{\mathcal{H}} - \left(\frac{x_{\text{B}}}{2}F_1 + \frac{t}{4M_p^2}F_2\right)\frac{x_{\text{B}}}{2}\widetilde{\mathcal{E}} + \frac{x_{\text{B}}}{2}(F_1 + F_2)\mathcal{H}. \tag{31}$$

- The first even harmonic of the single transverse-target spin asymmetry (15) and first odd harmonic of the double transverse-target spin asymmetry (17) in the charge-odd sector,

$$A_{\text{UT,I}}^{\sin(\varphi)\cos(1\phi)} \propto -\frac{\sqrt{1-y}}{2-y}\sqrt{\frac{M_p^2}{y^2 \mathcal{Q}^2}} \times x_{\text{B}} \, \mathfrak{Im}\left[\mathcal{C}_{\text{TP-}}^{\text{I}}(\mathcal{F}) + \cdots\right], \tag{32}$$

$$A_{\text{LT,I}}^{\sin(\varphi)\sin(1\phi)} \propto +\frac{y\sqrt{1-y}}{2-2y+y^2}\sqrt{\frac{M_p^2}{y^2 \mathcal{Q}^2}} \times x_{\text{B}} \, \mathfrak{Re}\left[\mathcal{C}_{\text{TP-}}^{\text{I}}(\mathcal{F}) + \cdots\right], \tag{33}$$

are *approximately* dominated by the imaginary and real part of the linear combination

$$\mathcal{C}_{\mathrm{TP-}}^{\mathrm{I}}(\mathcal{F}) \approx \frac{-t}{4M_p^2} \left[2F_2\mathcal{H} - 2F_1\mathcal{E} + x_{\mathrm{B}}(F_1 + F_2)\frac{x_{\mathrm{B}}}{2}\widetilde{\mathcal{E}} \right] + \cdots . \tag{34}$$

- The first odd harmonic of the single transverse-target spin asymmetry (15) and first even harmonic of the double transverse-target spin asymmetry (17) in the charge-odd sector,

$$A_{\mathrm{UT,I}}^{\cos(\varphi)\sin(1\phi)} \propto +\frac{\sqrt{1-y}}{2-y}\sqrt{\frac{M_p^2}{y^2\mathcal{Q}^2}} \times x_{\mathrm{B}} \, \mathfrak{Im} \left[\mathcal{C}_{\mathrm{TP+}}^{\mathrm{I}}(\mathcal{F}) + \cdots \right], \tag{35}$$

$$A_{\mathrm{LT,I}}^{\cos(\varphi)\cos(1\phi)} \propto +\frac{y\sqrt{1-y}}{2-2y+y^2}\sqrt{\frac{M_p^2}{y^2\mathcal{Q}^2}} \times x_{\mathrm{B}} \, \mathfrak{Re} \left[\mathcal{C}_{\mathrm{TP+}}^{\mathrm{I}}(\mathcal{F}) + \cdots \right], \tag{36}$$

are *approximately* dominated by the imaginary and real part of the linear combination

$$\mathcal{C}_{\mathrm{TP+}}^{\mathrm{I}}(\mathcal{F}) \approx \frac{-t}{4M_p^2} \left[2F_1\frac{x_{\mathrm{B}}}{2}\widetilde{\mathcal{E}} - 2F_2\widetilde{\mathcal{H}} \right] + \cdots . \tag{37}$$

As one realizes from the relations among observables and CFFs listed above, there are six linear combinations of CFFs: three for the imaginary parts (26,32,35) and three for the real parts (27,33,36). Unfortunately, the longitudinally polarized target double spin flip experiment has been performed only with positron beam and, hence, the asymmetries (29) and (30) are contaminated by twist-three contributions from the DVCS-squared term. Moreover, the latter term also depends on the first harmonic of the BH-squared term. Since the DVCS-squared contributions are expected to be relatively small and the first BH harmonic is suppressed for HERMES kinematics, the single spin and double spin flip asymmetries may be used to access the imaginary and real parts of the CFF combination (31). To get rid of these contaminations, we would need longitudinal single and double spin flip measurements in the charge odd sector which were unfortunately not performed[1].

Further twist-two dominated observables are the single transverse proton spin asymmetry and the double longitudinal-transverse spin asymmetry in the charge even sector:

- The zeroth harmonic of the single transverse target spin asymmetry, which is governed by the bilinear combination

$$A_{\mathrm{UT,DVCS}}^{\sin(\varphi)\cos(0\phi)} \propto +\frac{1-y}{4(2-y)}\frac{(-t)^{3/2}}{M_p\,y^2\mathcal{Q}^2} \times x_{\mathrm{B}}^2 \, \mathfrak{Im} \left[\mathcal{H}\mathcal{E}^* - \frac{x_{\mathrm{B}}}{2}\widetilde{\mathcal{H}}\widetilde{\mathcal{E}}^* \right], \tag{38}$$

- The zeroth harmonic of the double longitudinal-beam and transverse target spin asymmetry, which is dominated by the bilinear combination

$$A_{\mathrm{LT,BH+DVCS}}^{\cos(\varphi)\cos(0\phi)} \propto +\frac{y(1-y)}{4(2-2y+y^2)}\frac{(-t)^{3/2}}{M_p\,y^2\mathcal{Q}^2} \times x_{\mathrm{B}}^2 \, \mathfrak{Re} \left[\widetilde{\mathcal{H}}\mathcal{E}^* - \frac{x_{\mathrm{B}}}{2}\mathcal{H}\widetilde{\mathcal{E}}^* \right] + \mathrm{BH}^2 . \tag{39}$$

---

[1]For the history of the HERMES experiment see http://www-hermes.desy.de/hedt/seminar.html.

The asymmetry in (38) is a small quantity if the CFFs $\mathcal{H}$ and $\widetilde{\mathcal{H}}$ are nearly in phase with $\mathcal{E}$ and $\widetilde{\mathcal{E}}$, respectively. Interestingly, in asymmetry (39), CFFs with different parity are combined. We emphasize that for this longitudinal-transverse double spin asymmetry (39) the BH-squared term is, at HERMES, kinematically suppressed:

$$A_{\text{LT,BH+DVCS}}^{\cos(\varphi)\cos(0\phi)} \approx A_{\text{LT,DVCS}}^{\cos(\varphi)\cos(0\phi)} . \tag{40}$$

Similarly to the single spin asymmetry $A_{\text{UT,DVCS}}^{\sin(\varphi)\cos(0\phi)}$, this double spin asymmetry is therefore sensitive to the DVCS-squared term; this is demonstrated by the empty rectangles in the middle row of Fig. 4 that show the pure BH contribution. As mentioned above, the constant terms for charge odd asymmetries, which are relatively suppressed by $1/\mathcal{Q}$ w.r.t. the first harmonic, may also be dominated by twist-two associated CFFs; however, they may suffer from a larger contamination of effective twist-three CFFs, which are neglected here completely. Here we have available the real part of two linear combinations and the imaginary part of one:

- The zeroth harmonic of the beam charge asymmetry (12)

$$A_{\text{C}}^{\cos(0\phi)} \propto \frac{-t}{y\mathcal{Q}^2} \times x_{\text{B}}\,\mathfrak{Re}\left[\mathcal{C}_{\text{unp}}^{\text{I}}(\mathcal{F}) - \frac{(1-y)x_{\text{B}}}{2-2y+y^2}(F_1+F_2)\widetilde{\mathcal{H}} + \cdots\right]. \tag{41}$$

- The zeroth harmonic of the single and double transverse target flip asymmetries (15), and (17)

$$A_{\text{UT,I}}^{\sin(\varphi)\cos(0\phi)} \propto +\frac{\sqrt{-t}M_p}{y\mathcal{Q}^2} \times x_{\text{B}}\,\mathfrak{Im}\left[\mathcal{C}_{\text{TP-}}^{\text{I}}(\mathcal{F}) + \frac{(1-y)x_{\text{B}}}{2-2y+y^2}\frac{-t}{2M_p^2}(F_1+F_2)\frac{x_{\text{B}}}{2}\widetilde{\mathcal{E}}+\cdots\right], \tag{42}$$

$$A_{\text{LT,I}}^{\cos(\varphi)\cos(0\phi)} \propto -\frac{\sqrt{-t}M_p}{y\mathcal{Q}^2} \times x_{\text{B}}\,\mathfrak{Re}\left[\mathcal{C}_{\text{TP+}}^{\text{I}}(\mathcal{F}) + \frac{(1-y)x_{\text{B}}}{2-2y+y^2}\frac{-t}{2M_p^2}(F_1+F_2)\frac{x_{\text{B}}}{2}\widetilde{\mathcal{E}}+\cdots\right]. \tag{43}$$

Apart from terms that are kinematically suppressed at small x_{B} and large y, we realize that these asymmetries are already expressed in terms of CFF combinations (28, 34, 37) that determine the first harmonics. Hence these three asymmetries, measured by HERMES, may roughly expressed in terms of the first harmonics:

$$A_{\text{C}}^{\cos(0\phi)} \sim -\frac{\sqrt{-t}}{\mathcal{Q}}\frac{2-y}{\sqrt{1-y}}\,A_{\text{C}}^{\cos(1\phi)}, \tag{44}$$

$$A_{\text{UT,I}}^{\sin(\varphi)\cos(0\phi)} \sim -\frac{\sqrt{-t}}{\mathcal{Q}}\frac{2-y}{\sqrt{1-y}}\,A_{\text{UT,I}}^{\sin(\varphi)\cos(1\phi)}, \tag{45}$$

$$A_{\text{LT,I}}^{\cos(\varphi)\cos(0\phi)} \sim -\frac{\sqrt{-t}}{\mathcal{Q}}\frac{2-y}{\sqrt{1-y}}\,A_{\text{UT,I}}^{\cos(\varphi)\cos(1\phi)}, \tag{46}$$

where a fourth relation of the same form exists for the double longitudinal spin asymmetry, see (30) and (48) below. Note that the accuracy of these crude relations can be drastically improved
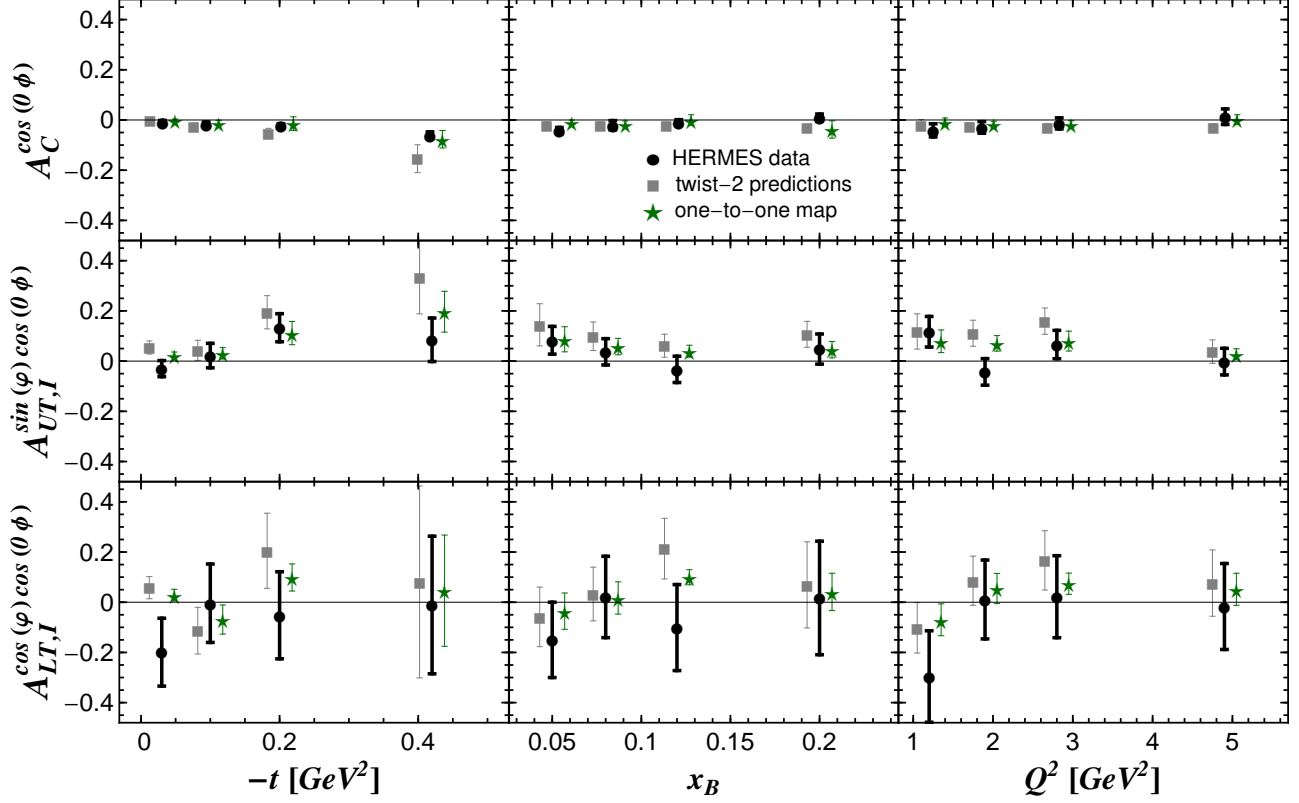
Figure 3: Expectations (squares, slightly shifted to the left) from the approximations (44–46) and values extracted from the one-to-one map (stars, slightly shifted to the right) are compared to the HERMES measurements (circles) of $A_{\mathrm{C}}^{\cos(0\phi)}$ (top), $A_{\mathrm{UT,I}}^{\sin(\varphi)\cos(0\phi)}$ (middle), and $A_{\mathrm{LT,I}}^{\cos(\varphi)\cos(0\phi)}$ (down) asymmetries in 12 bins by means.

by taking the higher BH harmonics into consideration. The relations among the charge odd asymmetries (44–46) offer an experimental consistency check of the underlying formalism, which is shown in Fig. 3. It can be seen that the expectations (squares) of our rough approximations (44–46) are mostly satisfied, where the largest deviation of $\sim 2\sigma$ appears in the 10th bin of $A_{\mathrm{UT,I}}^{\sin(\varphi)\cos(0\phi)}$. Unfortunately, the double spin asymmetries $A_{\mathrm{LT,I}}^{\cos(\varphi)\cos(0\phi)}$ and $A_{\mathrm{LT,I}}^{\cos(\varphi)\cos(1\phi)}$ suffer from limited statistics.

Another experimental test of the BH dominance is provided by:

- The zeroth harmonic of the longitudinally double spin flip asymmetry (14)

$$A_{\mathrm{LL,+}}^{\cos(0\phi)} = A_{\mathrm{LL,BH}}^{\cos(0\phi)} + A_{\mathrm{LL,I}}^{\cos(0\phi)} + A_{\mathrm{LL,DVCS}}^{\cos(0\phi)}, \qquad (47)$$

which is decomposed in its charge odd part,

$$A_{\mathrm{LL,I}}^{\cos(0\phi)} \propto +\frac{2-y}{2-2y+y^2}\frac{-t}{y\mathcal{Q}^2} \times x_{\mathrm{B}}\,\mathfrak{Re}\left[\mathcal{C}_{\mathrm{LP}}^{\mathrm{I}}(\mathcal{F}) + \frac{(1-y)x_{\mathrm{B}}}{(2-y)^2}(F_1+F_2)\mathcal{H} + \cdots\right], \quad (48)$$
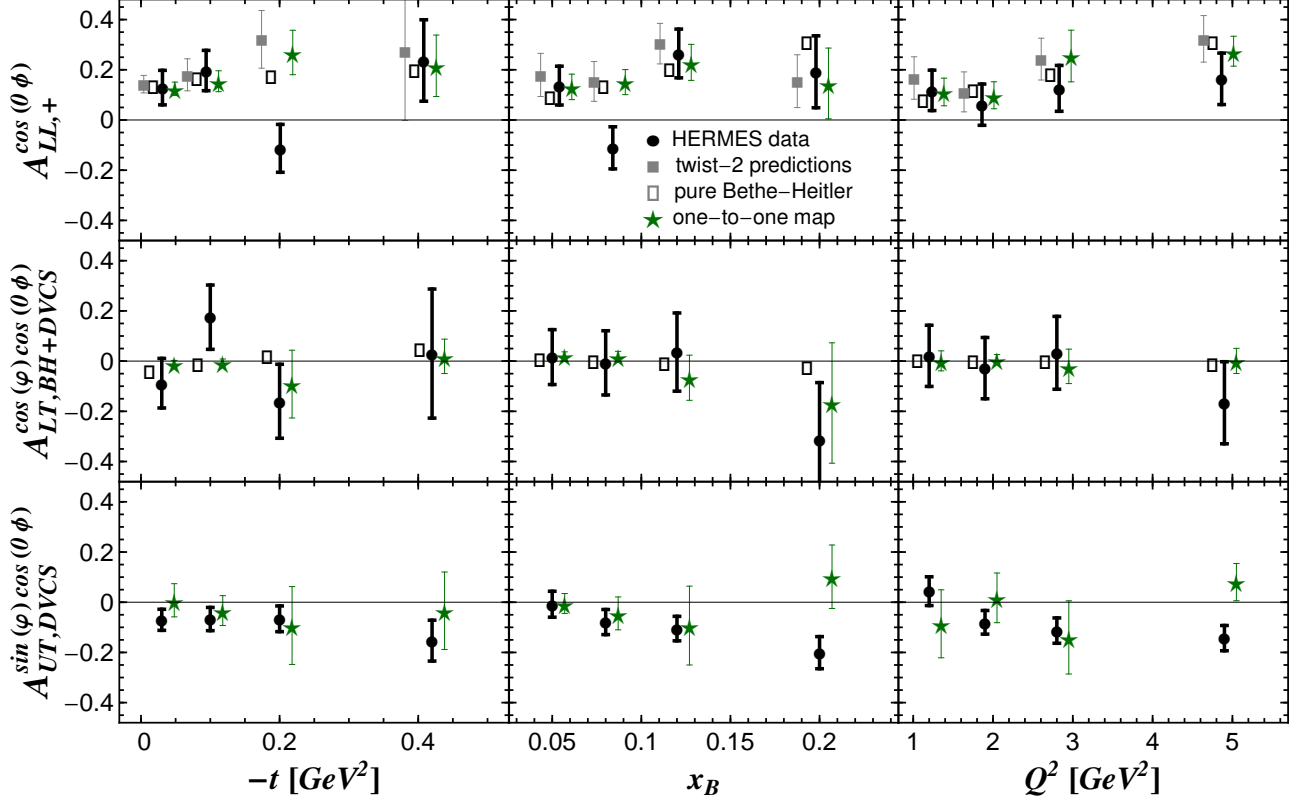
14

Figure 4: HERMES measurements of the double spin flip asymmetries $A_{\mathrm{LL},+}^{\cos(0\phi)}$ (top row) and $A_{\mathrm{LT,BH+DVCS}}^{\cos(\varphi)\cos(0\phi)}$ (middle row), as well as of the transverse single proton spin asymmetry $A_{\mathrm{UT,DVCS}}^{\sin(\varphi)\cos(0\phi)}$ (bottom row) in the charge even sector are displayed as circles. The measurements are compared with pure BH contributions (empty rectangles, slightly shifted to the left), expectations from the approximation (50) (squares, shifted to the left) and values extracted from the one-to-one map (stars, slightly shifted to the right).

and the charge even part, where the DVCS induced asymmetry part can be safely dropped,

$$A_{\mathrm{LL,BH+DVCS}}^{\cos(0\phi)} \approx A_{\mathrm{LL,BH}}^{\cos(0\phi)} . \tag{49}$$

For HERMES measurements, the relations (29, 47–49) yield the expectation

$$A_{\mathrm{LL},+}^{\cos(0\phi)} \approx A_{\mathrm{LL,BH}}^{\cos(0\phi)} - \sqrt{\frac{-t}{y^2\mathcal{Q}^2}}\frac{2-y}{\sqrt{1-y}}\left[A_{\mathrm{LL},+}^{\cos(1\phi)} - A_{\mathrm{LL,BH}}^{\cos(1\phi)}\right], \tag{50}$$

which is visualized in the upper panels of Fig. 4. It can be seen that the expectations (squares) of our rough approximation (50) are satisfied, except in the third and sixth bins. Note that if we take these bins literally, we have to conclude that in these two cases the DVCS amplitude overwhelms the BH amplitude and so the sign expected from the BH term changes. Perhaps more realistically, we may view these two bins simply as a statistical fluctuation on the $\sim 2\sigma$ level.

3.2 Methods for analyzing DVCS data

The amplitudes of the harmonics for the various asymmetries, extracted by the HERMES collaboration, can be analyzed in various manners, e.g., one may consider any of the following strategies.

i. CFFs are locally extracted from a complete set of observables by a map.

ii. CFFs are locally extracted by means of least squares, likelihood, or neural network fits.

iii. Comparing measurements with model predictions.

iv. Global model fits based on the least squares method, maximum-likelihood estimation, or neural networks.

The term *local* refers here to a three dimensional kinematical data point (bin) given by a x_{B}, t, and $\mathcal{Q}^2$ value. The first method has been proposed and discussed in [14], however, it has not been applied so far. Local extraction of the imaginary and real parts of CFFs (which, for brevity, we will call sub-CFFs) by means of least squares fits were applied to HERMES and JLAB data [23, 24, 25]. However, although called model-independent, these analysis are biased, too, by utilizing the hypothesis that seven sub-CFFs determine all harmonics and satisfy some model constraints. Both methods require that the observables have been measured in a common set of kinematic bins, where it is assumed that mean values of the kinematical variables are identical for all of the measurements. This, however, can be only approximately true. The kinematical condition can be relaxed if one employs neural networks. Presently, they have been employed to access the imaginary and real part of CFF $\mathcal{H}$ from HERMES data on unpolarized protons [26].

Model predictions for DVCS have existed for over a decade. In the beginning, it was rather popular to use Radyushin's double distribution ansatz (RDDA) for GPDs, given at $t = 0$ [27]. In this method, one uses information on parton distribution functions (PDFs) and form factors to build the model, while the GPD arises from a skewing operation that is governed by a profile function and the width of this concave function is controlled by a "b" parameter. Such models, e.g. given in [28], have been privately distributed as numerical code, referred according to the author names of the paper [29] as VGG, and it is often used to compare data with model predictions. However, when this is done, authors often neglect to give full details of the code version and precise details of the underlying model, e.g. the set of PDFs that are used to constrain the GPDs. The same underlying double-distribution ansatz was also used in the BMK model [14], in the numerical code of Freund-McDermott [30], and the Goloskokov-Kroll model [31, 32], used in an adjusted hand-bag model framework for the description of deeply virtual meson production. Certainly there are differences in all these models, however, since these models imply

H dominance and H is inherited from a unpolarized PDF parametrization and sometimes from the t-dependence of electromagnetic nucleon form factors, it is not very surprising that all these models applied to DVCS off unpolarized protons show similar features in a LO analysis. When describing to some extent present DVCS measurements with a RDDA based GPD model, one may use a small skewness effect, use in a LO analysis NLO PDF parameterizations and neglect GPD evolution (important in H1/ZEUS Collider kinematics). Aiming to describe DVCS data, it has been also suggested to build "flexible" GPD parameterization by violating their spectral (or polynomiality) property [33] (see also [34], where the claim of satisfying polynomiality is simply not true). This is an entirely unacceptable recipe (see comments in [35] and [36]) and so the phenomenological aspects of such models cannot be discussed.

Since it was widely realized in the past that most variations of the RDDA usually overestimate the size of beam spin asymmetries and do not describe some other observables, it was necessary to build flexible GPD models which can be used in numerical fast fitting routines [37, 38], where GPDs are modelled in terms of their conformal moments [39] (related representations were suggested in [40, 41, 42]). Thereby, one tries initially to parameterise the partonic degrees of freedom in such a manner that they are accessible from the experimental measurements. We will provide more details in Sect. 3.4.

We emphasize that one major impediment to the understanding of DVCS data in terms of one specific double-distribution ansatz is the lack of exclusivity in the data. As noted in section 2.2, there is an estimated average of 12% contamination of the HERMES data by processes involving an intermediate Δ-resonance. While HERMES has published a beam-helicity measurement from a very pure sample [18] that indicates that this contamination only acts as a small dilution of the asymmetry magnitude at higher values of $-t$ (e.g. $-t > 0.25\,\mathrm{GeV}^2$), there is sufficient uncertainty that one cannot make any definitive statements on the specific form of a double-distribution ansatz.

In the next section we outline the method of mapping the asymmetries to CFFs. Thereby we consider the asymmetries as normally distributed random variables and consider the extraction problem of CFFs simply as a map of random variables, where the functional dependence of asymmetries on CFFs is provided by the theory. In fact, for normally distributed random variables the formalism we employ is very well known from (non-)linear regression and we need only to discuss the maps of means and variances rather than probability distributions.

3.2.1 Maps of normally distributed random variables

Let us first clarify what we call the twist-two dominance hypothesis and the additional approximation that arise from a linearization procedure. For instance, the first harmonic of the beam

spin asymmetry (22) in the charge odd sector reads

$$A_{\rm LU,I}^{\sin(1\phi)} \simeq \frac{1}{\pi} \int_{-\pi}^{\pi} d\phi \, \sin(\phi) \tag{51}$$

$$\times \left. \frac{\hat{s}_1^{\rm I} \sin(\phi) + 0 \times \hat{s}_2^{\rm I} \sin(2\phi)}{\sum_{n=0}^{2} \hat{c}_n^{\rm BH} \cos(n\phi) + \frac{-t}{y^2 \mathcal{Q}^2} w(\phi) \hat{c}_0^{\rm DVCS} + 0 \times \frac{-t}{y^2 \mathcal{Q}^2} w(\phi) \sum_{n=1}^{2} \hat{c}_n^{\rm DVCS} \cos(n\phi)} \right|_{\mathcal{H}_{\rm eff} = \mathcal{H}_{\rm T} = 0},$$

where $0 \times \cdots$ indicate the expressions that are induced by twist-three and transversity contributions and are neglected. Note that the power suppressed admixture of $\mathcal{H}$ in the second odd harmonic is consequently neglected, too, and that we also alter the definition of the $\hat{c}_0^{\rm DVCS}$ coefficient, since power suppressed twist-three square terms and presumably-small transversity square terms are set to zero, cf. formula (2.18) in [16]. In this approximation the Fourier transform (51) can be evaluated in terms of elementary functions,

$$A_{\rm LU,I}^{\sin(1\phi)} \simeq \frac{N \hat{s}_1^{\rm I}}{\hat{c}_0^{\rm BH}} \times \frac{1}{b} \left(\sqrt{\frac{a^2 - 4b \left(1 + b + \sqrt{(1+b)^2 - a^2}\right)}{a^2 - 8(1-b)b}} - 1 \right), \tag{52}$$

where

$$N = \frac{\hat{c}_0^{\rm BH}}{\hat{c}_0^{\rm BH} + \frac{-t}{y^2 \mathcal{Q}^2} \hat{c}_0^{\rm DVCS}} \tag{53}$$

is considered as an overall normalization factor and the coefficients

$$a = \frac{\hat{c}_1^{\rm BH} + \frac{-t}{y^2 \mathcal{Q}^2} w_1 \hat{c}_0^{\rm DVCS}}{\hat{c}_0^{\rm BH} + \frac{-t}{y^2 \mathcal{Q}^2} \hat{c}_0^{\rm DVCS}} \stackrel{\rm BH>DVCS}{\approx} \frac{\hat{c}_1^{\rm BH}}{\hat{c}_0^{\rm BH}} \quad \text{and} \quad b = \frac{\hat{c}_2^{\rm BH} + \frac{-t}{y^2 \mathcal{Q}^2} w_2 \hat{c}_0^{\rm DVCS}}{\hat{c}_0^{\rm BH} + \frac{-t}{y^2 \mathcal{Q}^2} \hat{c}_0^{\rm DVCS}} \stackrel{\rm BH>DVCS}{\approx} \frac{\hat{c}_2^{\rm BH}}{\hat{c}_0^{\rm BH}} \tag{54}$$

arise from the higher harmonics of the denominator in (51). In our case of interest they satisfy the condition $|a| > |b|$, they are small quantities, and the indicated approximation (54) can be considered as justified in a BH dominated regime. Consequently, in such an approximation the DVCS-squared term enters only in the overall normalization factor N. Analogous formulae can be also obtained for even harmonics, where we restrict ourselves here to the two lowest harmonics.

Before we discuss the proton case, let us provide a pedagogical example with a spin-zero target. In this case we are dealing with three CFFs $\mathcal{H}$, $\mathcal{H}_{\rm eff}$, and $\mathcal{H}_{\rm T}$. Moreover, we assume that the second and third harmonics are compatible with zero, which suggest that the CFFs $\mathcal{H}_{\rm eff}$ and $\mathcal{H}_{\rm T}$, associated with partonic twist-three and transversity processes, can be neglected. Note that this approximation may induce an ambiguity in the phenomenological treatment; instead of neglecting $\mathcal{H}_{\rm eff}$ it may be alternatively justified to neglect the twist-three CFF $\mathcal{H}_3$, i.e., one

sets $\mathcal{H}_{\mathrm{eff}} \approx -x_{\mathrm{B}}\mathcal{H}$. We relate the dominant asymmetries to the twist-two associated CFF $\mathcal{H}$ by two linearized equations

$$A_{\mathrm{LU,I}}^{\sin(1\phi)} \approx N c_{\mathfrak{Im}}^{-1} \mathcal{H}^{\mathfrak{Im}} \quad \text{and} \quad A_{\mathrm{C}}^{\cos(1\phi)} \approx N c_{\mathfrak{Re}}^{-1} \mathcal{H}^{\mathfrak{Re}}, \tag{55}$$

where we use for later convenience the shorthands $\mathcal{H}^{\mathfrak{Im}} = \mathfrak{Im}\,\mathcal{H}$ and $\mathcal{H}^{\mathfrak{Re}} = \mathfrak{Re}\,\mathcal{H}$. The coefficients

$$c_{\mathfrak{Im}}^{-1} = \left.\frac{\partial A_{\mathrm{LU,I}}^{\sin(1\phi)}}{\partial \mathcal{H}^{\mathfrak{Im}}}\right|_{\mathcal{F}=0} \quad \text{and} \quad c_{\mathfrak{Re}}^{-1} = \left.\frac{\partial A_{\mathrm{C}}^{\cos(1\phi)}}{\partial \mathcal{H}^{\mathfrak{Re}}}\right|_{\mathcal{F}=0} \tag{56}$$

are calculated from (22,24) and (23,25) and are given as elementary functions of the Fourier coefficients s_1^{I}, c_1^{I}, and c_n^{BH}. In this procedure, we set the DVCS-squared term in the denominator to zero which, however, appears in the normalization factor N. This overall factor can be considered as a bilinear function of the twist-two associated CFF $\mathcal{H}$ or equivalently as a function of the asymmetries. To a good approximation, it can be also expressed by the ratio of the BH and DVCS cross sections

$$0 \lesssim N(\boldsymbol{A}) \approx \frac{\int_{-\pi}^{\pi} d\phi\, w(\phi) d\sigma_{\mathrm{BH}}(\phi)}{\int_{-\pi}^{\pi} d\phi\, w(\phi)\left[d\sigma_{\mathrm{BH}}(\phi) + d\sigma_{\mathrm{DVCS}}(\phi)\right]} \lesssim 1. \tag{57}$$

The solution of the linearized equations (55) is immediately obtained and, with our twist-two dominance assumption, the imaginary and real part of the leading twist-two associated CFF reads

$$\mathfrak{Im}\,\mathcal{H} = \frac{c_{\mathfrak{Im}}}{N(\boldsymbol{A})} A_{\mathrm{LU,I}}^{\sin(1\phi)} \quad \text{and} \quad \mathfrak{Re}\,\mathcal{H} = \frac{c_{\mathfrak{Re}}}{N(\boldsymbol{A})} A_{\mathrm{C}}^{\cos(1\phi)}, \tag{58}$$

where $c_{\mathfrak{Im}}$ and $c_{\mathfrak{Re}}$ represent now two numbers for a given kinematical point. The normalization factor is approximately given as

$$N \approx \frac{1}{1 + \frac{k}{4}|\mathcal{H}|^2} \quad \text{with} \quad \frac{k}{4}|\mathcal{H}|^2 = \left.\frac{\int_{-\pi}^{\pi} d\phi\, w(\phi) d\sigma_{\mathrm{DVCS}}(\phi)}{\int_{-\pi}^{\pi} d\phi\, w(\phi) d\sigma_{\mathrm{BH}}(\phi)}\right|_{\mathcal{H}_{\mathrm{eff}}=\mathcal{H}_{\mathrm{T}}=0}, \tag{59}$$

where k is a known kinematical factor. Plugging the solution (58) into the normalization (59) yields a cubic equation in N that has two non-trivial solutions:

$$N(\boldsymbol{A}) \approx \frac{1}{2}\left(1 \pm \sqrt{1 - k\, c_{\mathfrak{Im}}^2 \left(A_{\mathrm{LU,I}}^{\sin(1\phi)}\right)^2 - k\, c_{\mathfrak{Re}}^2 \left(A_{\mathrm{C}}^{\cos(1\phi)}\right)^2}\right). \tag{60}$$

The solution with the positive root satisfies the boundary condition $N(\boldsymbol{A}=\boldsymbol{0}) = 1$ and is the one to take if the BH amplitude overwhelms the DVCS one. Obviously, the solution with the negative root satisfies the boundary condition $N(\boldsymbol{A}=\boldsymbol{0}) = 0$ and it is the one to take if the

unpolarized DVCS cross section is larger than the BH one. Finally, error propagation is done in the common manner. If the experimental errors are uncorrelated, we may write the relative standard error in the following form

$$\frac{(\delta\,\mathfrak{Im}\,\mathcal{H})^2}{|\,\mathfrak{Im}\,\mathcal{H}|^2} = \frac{\left(\delta A_{\mathrm{LU,I}}^{\sin(1\phi)}\right)^2}{\left(A_{\mathrm{LU,I}}^{\sin(1\phi)}\right)^2} + \frac{(\delta N)^2}{N^2} - 2\frac{\partial N}{N\partial A_{\mathrm{LU,I}}^{\sin(1\phi)}}\frac{1}{A_{\mathrm{LU,I}}^{\sin(1\phi)}}\left(\delta A_{\mathrm{LU,I}}^{\sin(1\phi)}\right)^2, \tag{61}$$

$$\frac{(\delta\,\mathfrak{Re}\,\mathcal{H})^2}{|\,\mathfrak{Re}\,\mathcal{H}|^2} = \frac{\left(\delta A_{\mathrm{C}}^{\cos(1\phi)}\right)^2}{\left(A_{\mathrm{C}}^{\cos(1\phi)}\right)^2} + \frac{(\delta N)^2}{N^2} - 2\frac{\partial N}{N\partial A_{\mathrm{C}}^{\cos(1\phi)}}\frac{1}{A_{\mathrm{C}}^{\cos(1\phi)}}\left(\delta A_{\mathrm{C}}^{\cos(1\phi)}\right)^2, \tag{62}$$

where the normalization uncertainty,

$$\frac{(\delta N)^2}{N^2} = \left|\frac{\partial N}{N\partial A_{\mathrm{LU,I}}^{\sin(1\phi)}}\right|^2 \left(\delta A_{\mathrm{LU,I}}^{\sin(1\phi)}\right)^2 + \left|\frac{\partial N}{N\partial A_{\mathrm{C}}^{\cos(1\phi)}}\right|^2 \left(\delta A_{\mathrm{C}}^{\cos(1\phi)}\right)^2 + \cdots, \tag{63}$$

can be easily evaluated by means of (60) and one may add a model estimate due to the neglected twist-three and other transversity CFFs, which is indicated by the ellipsis.

The method, i.e., the map of random variables, can be refined by the inclusion of higher harmonics and it can be extended to a nucleon target. According to the experimental observables and the assumptions, we have generically a set of charge-odd asymmetries, arising from the interference of BH and DVCS amplitudes, that we arrange into an m–dimensional vector:

$$\left(\boldsymbol{A}^{\mathcal{I}}\right)^{\mathsf{T}} = (A_1, \cdots, A_m) . \tag{64}$$

For a complete twist-two DVCS off-the-nucleon analysis, we need 4 even and 4 odd harmonics. Inclusion of the twist-three sector increases the number of harmonics to 16, while for an hypothesis-free treatment we need 24 asymmetries. Surely hypotheses can be refined, e.g., in [23] the assumption $\mathfrak{Im}\,\widetilde{\mathcal{E}} = 0$ is made in a twist-two analysis. Up to an overall normalization, we can formulate a linear mapping problem as follows:

$$\boldsymbol{A}^{\mathcal{I}} = N\big(\boldsymbol{A}^{\mathcal{I}}|\boldsymbol{\mathcal{G}}\big)\,\boldsymbol{c}^{-1}\cdot\boldsymbol{\mathcal{F}} + N\big(\boldsymbol{A}^{\mathcal{I}}|\boldsymbol{\mathcal{G}}\big)\,\boldsymbol{b}\cdot\boldsymbol{\mathcal{G}}, \tag{65}$$

where $\boldsymbol{\mathcal{F}}$ is the set of sub-CFFs (written as an m–dimensional vector) that one wants to extract from the measurements and $\boldsymbol{\mathcal{G}}$ is the set of sub-CFFs that is considered as inaccessible within a given hypothesis. The inverse $m \times m$ coefficient matrix $\boldsymbol{c}^{-1}$ and $m \times (n-m)$ matrix $\boldsymbol{b}$ of the inhomogeneous term are calculated from the theoretical formulae, e.g., for asymmetries proportional to the interference term, we may use

$$\boldsymbol{c}^{-1} = \frac{\partial\boldsymbol{A}^{\mathcal{I}}}{\partial\boldsymbol{\mathcal{F}}}\bigg|_{\boldsymbol{\mathcal{F}}=\boldsymbol{\mathcal{G}}=0} \quad \text{and} \quad \boldsymbol{b} = \frac{\partial\boldsymbol{A}^{\mathcal{I}}}{\partial\boldsymbol{\mathcal{G}}}\bigg|_{\boldsymbol{\mathcal{F}}=\boldsymbol{\mathcal{G}}=0}. \tag{66}$$

Obviously, the solution of the inhomogeneous problem (65) provides us the sub-CFFs $\mathcal{F}$ in dependence on the m observables $\boldsymbol{A}^{\mathcal{I}}$ and the $(n-m)$ dimensional set of unknown sub-CFFs $\boldsymbol{\mathcal{G}}$:

$$\mathcal{F} = \frac{1}{N(\boldsymbol{A}^{\mathcal{I}}|\boldsymbol{\mathcal{G}})}\boldsymbol{c} \cdot \boldsymbol{A}^{\mathcal{I}} - \boldsymbol{c} \cdot \boldsymbol{b} \cdot \boldsymbol{\mathcal{G}}. \tag{67}$$

The variation of the solution w.r.t. both the measurement and the unknown sub-CFFs can be written in terms of an $m \times m$ matrix and an $m \times (n-m)$ matrix

$$\frac{\partial \mathcal{F}}{\partial \boldsymbol{A}^{\mathcal{I}}} = \frac{1}{N(\boldsymbol{A}^{\mathcal{I}}|\boldsymbol{\mathcal{G}})}\left[\boldsymbol{c} - \frac{\boldsymbol{c} \cdot \boldsymbol{A}^{\mathcal{I}}}{N(\boldsymbol{A}^{\mathcal{I}}|\boldsymbol{\mathcal{G}})} \otimes \frac{\partial N(\boldsymbol{A}^{\mathcal{I}}|\boldsymbol{\mathcal{G}})}{\partial \boldsymbol{A}^{\mathcal{I}}}\right], \tag{68}$$

$$\frac{\partial \mathcal{F}}{\partial \boldsymbol{\mathcal{G}}} = -\frac{\boldsymbol{c} \cdot \boldsymbol{A}^{\mathcal{I}}}{N^2(\boldsymbol{A}^{\mathcal{I}}|\boldsymbol{\mathcal{G}})} \otimes \frac{\partial N(\boldsymbol{A}^{\mathcal{I}}|\boldsymbol{\mathcal{G}})}{\partial \boldsymbol{\mathcal{G}}} - \boldsymbol{c} \cdot \boldsymbol{b}, \tag{69}$$

where $\otimes$ symbolizes the direct product of two vectors, e.g.,

$$\left\{\boldsymbol{\mathcal{A}} \otimes \frac{\partial N}{N\partial \boldsymbol{\mathcal{G}}}\right\}_{ab} = \boldsymbol{\mathcal{A}}_a \frac{1}{N}\frac{\partial N}{\partial \boldsymbol{\mathcal{G}}_b}, \quad a, b \in \{1, \cdots, m\}, \quad b \in \{1, \cdots, n-m\}.$$

In the case that (with a given hypothesis) the number of sub-CFFs matches the numbers of observables, our equation (65) reduces to a homogenous one, i.e., we can set the inhomogeneous term in (67), containing the matrix $\boldsymbol{b}$, to zero and the variation of the solution is given by the Jacobian (68), which can be now written in the form

$$\frac{\partial \mathcal{F}}{\partial \boldsymbol{A}^{\mathcal{I}}} = \frac{1}{N(\boldsymbol{A}^{\mathcal{I}})}\left[\boldsymbol{c} - \mathcal{F} \otimes \frac{\partial N(\boldsymbol{A}^{\mathcal{I}})}{\partial \boldsymbol{A}^{\mathcal{I}}}\right]. \tag{70}$$

From this we can easily transform the (variance-)covariance matrix of the experimental measurements to that of sub-CFFs:

$$\mathrm{cov}(\mathcal{F}) = \left[\frac{\partial \mathcal{F}}{\partial \boldsymbol{A}^{\mathcal{I}}}\right] \cdot \mathrm{cov}\left(\boldsymbol{A}^{\mathcal{I}}\right) \cdot \left[\frac{\partial \mathcal{F}}{\partial \boldsymbol{A}^{\mathcal{I}}}\right]^{\mathsf{T}}, \tag{71}$$

where the result reads more explicitly as

$$\begin{aligned}
\mathrm{cov}(\mathcal{F}) = {} & \frac{1}{N^2}\boldsymbol{c} \cdot \mathrm{cov}\left(\boldsymbol{A}^{\mathcal{I}}\right) \cdot \boldsymbol{c}^{\mathsf{T}} \\
& - \frac{1}{N}\left[\boldsymbol{c} \cdot \mathrm{cov}\left(\boldsymbol{A}^{\mathcal{I}}\right) \cdot \left(\mathcal{F} \otimes \frac{\partial N(\boldsymbol{A}^{\mathcal{I}})}{N\partial \boldsymbol{A}^{\mathcal{I}}}\right)^{\mathsf{T}} + \left(\mathcal{F} \otimes \frac{\partial N(\boldsymbol{A}^{\mathcal{I}})}{N\partial \boldsymbol{A}^{\mathcal{I}}}\right) \cdot \mathrm{cov}\left(\boldsymbol{A}^{\mathcal{I}}\right) \cdot \boldsymbol{c}^{\mathsf{T}}\right] \\
& + \left(\mathcal{F} \otimes \frac{\partial N(\boldsymbol{A}^{\mathcal{I}})}{N\partial \boldsymbol{A}^{\mathcal{I}}}\right) \cdot \mathrm{cov}\left(\boldsymbol{A}^{\mathcal{I}}\right) \cdot \left(\mathcal{F} \otimes \frac{\partial N(\boldsymbol{A}^{\mathcal{I}})}{N\partial \boldsymbol{A}^{\mathcal{I}}}\right)^{\mathsf{T}}.
\end{aligned} \tag{72}$$

This representation allows us to discuss separately the overall normalization error given by the last term on the r.h.s. of this equation. The normalization factor N is determined as in our toy example from substituting the resultant sub-CFFs into (57), which provides again a cubic

21

equation for N. The correct solution is picked up by the requirement that N is real valued, lies in the interval $0 < N < 1$, and from the knowledge if the observables arise from a BH ($N > 1/2$) or DVCS ($N < 1/2$) dominated scenario. If such a solution does not exist, e.g. due to some large statistical fluctuation of a mean value, the mapping method is strictly-speaking not applicable; however, as we will see below in Sect. 3.3.1 in some of such cases it can be still considered as a useful tool.

If no further experimental information in a given kinematical bin is available, one may use a model estimate for the remaining unknown sub-CFFs $\mathcal{G}$ and propagate the estimated uncertainties by means of a covariance matrix, providing us with the sum

$$\mathrm{cov}(\mathcal{F}) = \left[\frac{\partial \mathcal{F}}{\partial \mathbf{A}}\right] \cdot \mathrm{cov}\left(\mathbf{A}\right) \cdot \left[\frac{\partial \mathcal{F}}{\partial \mathbf{A}}\right]^{\mathsf{T}} + \left[\frac{\partial \mathcal{F}}{\partial \mathcal{G}}\right] \cdot \mathrm{cov}\left(\mathcal{G}\right) \cdot \left[\frac{\partial \mathcal{F}}{\partial \mathcal{G}}\right]^{\mathsf{T}} . \tag{73}$$

A more appropriate method would be to constrain the uniformly randomly distributed values of unknown sub-CFFs $\mathcal{G}$ and propagate the uncertainties numerically to the errors of the extracted sub-CFFs $\mathcal{F}$, formally written as

$$\mathcal{F} = \left\langle \frac{1}{N(\mathbf{A}|\mathcal{G})} \mathbf{c} \cdot \mathbf{A} - \mathbf{c} \cdot \mathbf{b} \cdot \mathcal{G} \right\rangle, \tag{74}$$

$$\frac{\partial \mathcal{F}}{\partial \mathbf{A}} = \left\langle \frac{1}{N(\mathbf{A}|\mathcal{G})} \left[\mathbf{c} - \frac{\mathbf{c} \cdot \mathbf{A}^{\mathcal{I}}}{N(\mathbf{A}^{\mathcal{I}}|\mathcal{G})} \otimes \frac{\partial N(\mathbf{A}|\mathcal{G})}{\partial \mathbf{A}} \right] \right\rangle. \tag{75}$$

A third possibility is that the remaining unknown sub-CFFs $\mathcal{G}$ could be extracted from asymmetries in the charge odd sector, i.e., related to the DVCS-squared term. Let us arrange these asymmetries as an $n - m$ dimensional vector

$$(\mathbf{A}^{\mathrm{DVCS}})^{\mathsf{T}} = (A_{m+1}, \cdots, A_n) , \tag{76}$$

and let us suppose that we can complete the number of observables, written now in terms of a n dimensional vector

$$\mathbf{A}^{\mathsf{T}} = (A_1, \cdots, A_m, A_{m+1}, \cdots, A_n) . \tag{77}$$

The charge-even observables are linear or quadratic in the remaining sub-CFFs $\mathcal{G}$, i.e., they are constrained by a system of linear constraints,

$$A_i^{\mathrm{DVCS}} = N(\mathbf{A}) \, \mathbf{b}_i^{\mathsf{T}}(\mathcal{F}) \cdot \mathcal{G}, \quad i \in \{m+1, \cdots, n\}, \tag{78}$$

such as those accessed by the transverse target spin asymmetry (38), or quadratic equations,

$$A_i^{\mathrm{DVCS}} = N(\mathcal{F}) \left[a_i(\mathcal{F}) + \mathbf{b}_i^{\mathsf{T}}(\mathcal{F}) \cdot \mathcal{G} + \mathcal{G}^{\mathsf{T}} \cdot \mathbf{c}_i \cdot \mathcal{G} \right], \quad i \in \{m+1, \cdots, n\}, \tag{79}$$

where the overall normalization can now be considered as a function of the complete set of asymmetries (77). Substituting the solutions of the linear constraints (67) into (78) and/or (79), one will generally end up with $n - m$ quadratic equations

$$A_i^{\mathrm{DVCS}} = N(\boldsymbol{A}) \left[\mathrm{a}_i(\boldsymbol{A}^{\mathcal{I}} | N(\boldsymbol{A})) + \mathbf{b}_i^{\mathsf{T}}(\boldsymbol{A}^{\mathcal{I}} | N(\boldsymbol{A})) \cdot \boldsymbol{\mathcal{G}} + \boldsymbol{\mathcal{G}}^{\mathsf{T}} \cdot \mathbf{c}_i(\boldsymbol{A}^{\mathcal{I}} | N(\boldsymbol{A})) \cdot \boldsymbol{\mathcal{G}} \right] , \tag{80}$$

where all coefficients explicitly depend only on the charge-odd asymmetries $\boldsymbol{A}^{\mathcal{I}}$ and the normalization factor N, which appears on the r.h.s. as N^p with $p \in \{-1, 0, 1\}$. The quadratic constraints (80) may be analytically solved, too, and the solution may be written for convenience in terms of a matrix equation

$$\boldsymbol{\mathcal{G}} = \frac{1}{N(\boldsymbol{A})} \, \boldsymbol{c}_{\mathrm{DVCS}}(\boldsymbol{A} | N(\boldsymbol{A})) \cdot \boldsymbol{A}^{\mathrm{DVCS}} , \tag{81}$$

where $\boldsymbol{c}_{\mathrm{DVCS}}$ is an $(n - m) \times (n - m)$ matrix that explicitly depends on the asymmetries and on the normalization, in general in a non-linear manner (containing roots). Of course, the solution (81) is not unique and only real-valued sub-CFFs are of interest. Moreover, one would naturally utilize boundary conditions to select the desired solution. Other disadvantages of using charge-even rather than charge-odd observables are that the former asymmetries are expected to be smaller than the latter ones and the $\boldsymbol{c}_{\mathrm{DVCS}}$ matrix is only known within some given experimental uncertainty. The gradient of the remaining sub-CFFs is calculated from

$$\frac{\partial \boldsymbol{\mathcal{G}}}{\partial \boldsymbol{A}} = \frac{1}{N(\boldsymbol{A})} \, \boldsymbol{c}_{\mathrm{DVCS}}(\boldsymbol{A}) \cdot \frac{\partial \boldsymbol{A}^{\mathrm{DVCS}}}{\partial \boldsymbol{A}} + \frac{1}{N(\boldsymbol{A})} \frac{\partial \boldsymbol{c}_{\mathrm{DVCS}}(\boldsymbol{A})}{\partial \boldsymbol{A}} \cdot \boldsymbol{A}^{\mathrm{DVCS}} - \boldsymbol{\mathcal{G}} \otimes \frac{\partial N(\boldsymbol{A})}{N(\boldsymbol{A}) \, \partial \boldsymbol{A}} , \tag{82}$$

where $\partial \boldsymbol{A}^{\mathrm{DVCS}} / \partial \boldsymbol{A}$ is a $(n - m) \times n$ matrix that projects on the subspace of charge even asymmetries.

As we have shown, we can map, under certain assumptions, the measured observables into the (sub)space of CFFs. We may collect these into the vector

$$\boldsymbol{\mathcal{F}}^{\mathsf{T}} = (\mathcal{F}_1^{\mathfrak{Im}}, \cdots, \mathcal{F}_n^{\mathfrak{Im}}, \mathcal{F}_1^{\mathfrak{Re}}, \cdots, \mathcal{F}_n^{\mathfrak{Re}}) ,$$

where the sub-CFFs $\mathcal{G} \cdots, \mathcal{G}_{n-m}$ are now a part of $\mathcal{F}$ and n is now replaced by the number $2n$. Combining the linear and quadratic solutions (81) allows us to find these $2n$ sub-CFFs from the asymmetries by means of

$$\boldsymbol{\mathcal{F}} = \frac{1}{N(\boldsymbol{A})} \, \boldsymbol{c}(\boldsymbol{A} | N(\boldsymbol{A})) \cdot \boldsymbol{A} , \tag{83}$$

which can be non-linear in the measured asymmetries $\boldsymbol{A}$, specified as vectors in (77). The covariance matrix is calculated in the common manner as in (71), replace there $\boldsymbol{A}^{\mathcal{I}}$ by $\boldsymbol{A}$, where the gradient is now given as a $2n \times 2n$ matrix

$$\frac{\partial \boldsymbol{\mathcal{F}}}{\partial \boldsymbol{A}} = \frac{1}{N(\boldsymbol{A})} \left[\boldsymbol{c}(\boldsymbol{A}) + \frac{\partial \boldsymbol{c}(\boldsymbol{A})}{\partial \boldsymbol{A}} \cdot \boldsymbol{A} - \boldsymbol{\mathcal{F}} \otimes \frac{\partial N(\boldsymbol{A})}{\partial \boldsymbol{A}} \right] . \tag{84}$$

23

Let us recall that the normalization factor N as a function of the $2n$ asymmetry measurements follows from substituting the solution of (83) into the definition (57), which also allows us to calculate its gradient:

$$N(\boldsymbol{A}), \quad \frac{\partial N(\boldsymbol{A})}{N\,\partial\boldsymbol{A}}. \tag{85}$$

Remaining observables that are not used for the extraction of CFFs can be evaluated from the solution (83) and may serve as a test for the validity of assumptions.

3.3 Local extraction of Compton form factors

As explained in the preceding section, the extraction of CFFs can be considered as a map of random variables from the space of observables to the space of sub-CFFs rather than as a fitting problem in which one relies on a given model and tries to find its parameters by means of statistical methods. Of course, one may consider the theory as a model and use the least-squares method (or maximum likelihood estimation) to extract locally CFFs from measurements. In the following sections we use both points of view in local extraction procedures and confront the findings.

The fourteen HERMES measurements, which we will utilize in different variations, together with the definition of asymmetries, described in Sect. 3.1, are listed in Tab. 2. Naturally, we will arrange the selected asymmetries as a vector, e.g., an eight dimensional one $\boldsymbol{A}^{\intercal} = (A_1, \cdots, A_8)$. In our analyses we assume that experimental errors are normally distributed, and the error propagation is performed as described in Sect. 3.2.1. The correlations of experimental errors have not been analyzed to the full extent; however, the results for the overall values as published by the HERMES collaboration may suggest that the covariance matrix is mostly diagonal [22]. Thus, we may safely assume in the following that the experimental errors are uncorrelated, e.g., a eight-dimensional covariance matrix

$$\mathrm{cov}(\boldsymbol{A}) = \begin{pmatrix} \delta^2 A_1 & 0 & \cdots & \cdots & 0 \\ 0 & \delta^2 A_2 & 0 & \cdots & 0 \\ \vdots & \cdots & \ddots & \cdots & \vdots \\ 0 & \cdots & \cdots & \delta^2 A_7 & 0 \\ 0 & \cdots & \cdots & 0 & \delta^2 A_8 \end{pmatrix} \tag{86}$$

contains only diagonal entries, which for simplicity (actually, due to missing information we cannot do better) are given as the sums of squared statistical and systematic errors.

As there is no broad consensus for the precise definition of CFFs, we adopt here the conventions of [16] for unpolarized and longitudinally polarized target asymmetries and take for

24

Observable	Definition	Formulae	Data from ref.
$A_{\mathrm{LU,I}}^{\sin(1\phi)}$	$\int_{-\pi}^{\pi}\frac{d\phi\,\sin\phi}{\pi}A_{\mathrm{LU,I}}(\phi)$	(10) and (26,28)	[22], see Sect. 2.2
$A_{\mathrm{C}}^{\cos(1\phi)}$	$\int_{-\pi}^{\pi}\frac{d\phi\,\cos\phi}{\pi}A_{\mathrm{C}}(\phi)$	(12) and (27,28)	[22], see Sect. 2.2
$A_{\mathrm{C}}^{\cos(0\phi)}$	$\int_{-\pi}^{\pi}\frac{d\phi}{2\pi}A_{\mathrm{C}}(\phi)$	(12) and (41,28)	[22], see Sect. 2.2
$A_{\mathrm{UL,+}}^{\sin(1\phi)}$	$\int_{-\pi}^{\pi}\frac{d\phi\,\sin\phi}{\pi}A_{\mathrm{UL,+}}(\phi)$	(13) and (29,31)	Tab. 4 from [21]
$A_{\mathrm{LL,+}}^{\cos(1\phi)}$	$\int_{-\pi}^{\pi}\frac{d\phi\,\cos\phi}{\pi}A_{\mathrm{LL,+}}(\phi)$	(14) and (30,31)	Tab. 4 from [21]
$A_{\mathrm{LL,+}}^{\cos(0\phi)}$	$\int_{-\pi}^{\pi}\frac{d\phi}{2\pi}A_{\mathrm{LL,+}}(\phi)$	(14) and (47,48)	Tab. 4 from [21]
$A_{\mathrm{UT,I}}^{\sin(\varphi)\cos(1\phi)}$	$\int_{-\pi}^{\pi}\frac{d\varphi\,\sin\varphi}{\pi}\int_{-\pi}^{\pi}\frac{d\phi\,\cos\phi}{\pi}A_{\mathrm{UT,I}}(\phi,\varphi)$	(15) and (32,34)	Tab. 1b from [13]
$A_{\mathrm{UT,I}}^{\cos(\varphi)\sin(1\phi)}$	$\int_{-\pi}^{\pi}\frac{d\varphi\,\cos\varphi}{\pi}\int_{-\pi}^{\pi}\frac{d\phi\,\sin\phi}{\pi}A_{\mathrm{UT,I}}(\phi,\varphi)$	(15) and (35,37)	Tab. 1b from [13]
$A_{\mathrm{UT,DVCS}}^{\sin(\varphi)\cos(0\phi)}$	$\int_{-\pi}^{\pi}\frac{d\varphi\,\sin\varphi}{\pi}\int_{-\pi}^{\pi}\frac{d\phi}{2\pi}A_{\mathrm{UT,DVCS}}(\phi,\varphi)$	(16) and (38)	Tab. 1a from [13]
$A_{\mathrm{UT,I}}^{\sin(\varphi)\cos(0\phi)}$	$\int_{-\pi}^{\pi}\frac{d\varphi\,\sin\varphi}{\pi}\int_{-\pi}^{\pi}\frac{d\phi}{2\pi}A_{\mathrm{UT,I}}(\phi,\varphi)$	(15) and (42,34)	Tab. 1b from [13]
$A_{\mathrm{LT,I}}^{\sin(\varphi)\sin(1\phi)}$	$\int_{-\pi}^{\pi}\frac{d\varphi\,\sin\varphi}{\pi}\int_{-\pi}^{\pi}\frac{d\phi\,\sin\phi}{\pi}A_{\mathrm{LT,I}}(\phi,\varphi)$	(17) and (33,34)	Tab. 2 from [15]
$A_{\mathrm{LT,I}}^{\cos(\varphi)\cos(1\phi)}$	$\int_{-\pi}^{\pi}\frac{d\varphi\,\cos\varphi}{\pi}\int_{-\pi}^{\pi}\frac{d\phi\,\cos\phi}{\pi}A_{\mathrm{LT,I}}(\phi,\varphi)$	(17) and (36,37)	Tab. 2 from [15]
$A_{\mathrm{LT,BH+DVCS}}^{\cos(\varphi)\cos(0\phi)}$	$\int_{-\pi}^{\pi}\frac{d\varphi\,\cos\varphi}{\pi}\int_{-\pi}^{\pi}\frac{d\phi}{2\pi}A_{\mathrm{LT,even}}(\phi,\varphi)$	(18) and (39)	Tab. 3 from [15]
$A_{\mathrm{LT,I}}^{\cos(\varphi)\cos(0\phi)}$	$\int_{-\pi}^{\pi}\frac{d\varphi\,\cos\varphi}{\pi}\int_{-\pi}^{\pi}\frac{d\phi}{2\pi}A_{\mathrm{LT,I}}(\phi,\varphi)$	(17) and (43,37)	Tab. 2 from [15]

Table 2: Observables from HERMES measurements that are utilized for the extraction of twist-two associated CFFs.

transversally polarized ones the $1/\mathcal{Q}$ expanded expressions from [14]. Moreover, we will restrict ourselves here to the twist-two sector, i.e. to the CFFs $\mathcal{F} \in \{\mathcal{H}, \mathcal{E}, \widetilde{\mathcal{H}}, \widetilde{\mathcal{E}}\}$ related to the observables by setting the remaining eight CFFs $\mathcal{F}_{\mathrm{eff}}$ and $\mathcal{F}_{\mathrm{T}}$ to zero, which is justified by the fact that higher harmonics are compatible with zero or are difficult to interpret[2]. The imaginary and real parts of the twist-two associated CFFs $\mathcal{F}$ are collected in an eight dimensional vector

$$\mathcal{F}^{\intercal} = \left(\mathcal{H}^{\mathfrak{Im}}, \widetilde{\mathcal{H}}^{\mathfrak{Im}}, \mathcal{E}^{\mathfrak{Im}}, \overline{\mathcal{E}}^{\mathfrak{Im}}, \mathcal{H}^{\mathfrak{Re}}, \widetilde{\mathcal{H}}^{\mathfrak{Re}}, \mathcal{E}^{\mathfrak{Re}}, \overline{\mathcal{E}}^{\mathfrak{Re}}\right), \tag{87}$$

---

[2]In contrast to other higher harmonics, in the longitudinal single target asymmetry a relatively large $\sin(2\phi)$ moment with large uncertainties has been observed, which increases with growing $-t$ and which is maximally up to $\sim 2\sigma$ deviations away from zero [21]. However, this large value is concentrated in a single bin in the x_{B} projection, which is supportive of concluding that the amplitude is simply a fluctuation.

written below as $\boldsymbol{\mathcal{F}} = \begin{pmatrix} \boldsymbol{\mathcal{F}}^{\mathfrak{Im}} \\ \boldsymbol{\mathcal{F}}^{\mathfrak{Re}} \end{pmatrix}$ in terms of two four dimensional column vectors

$$\boldsymbol{\mathcal{F}}^{\mathfrak{Im}} = \mathfrak{Im}\begin{pmatrix} \mathcal{H} \\ \widetilde{\mathcal{H}} \\ \mathcal{E} \\ \overline{\mathcal{E}} \end{pmatrix} \quad \text{and} \quad \boldsymbol{\mathcal{F}}^{\mathfrak{Re}} = \mathfrak{Re}\begin{pmatrix} \mathcal{H} \\ \widetilde{\mathcal{H}} \\ \mathcal{E} \\ \overline{\mathcal{E}} \end{pmatrix}, \quad \text{where we use } \overline{\mathcal{E}} = \frac{x_{\mathrm{B}}}{2 - x_{\mathrm{B}}}\widetilde{\mathcal{E}}. \tag{88}$$

The (approximate) redefinition of $\widetilde{\mathcal{E}}$ into $\overline{\mathcal{E}}$ removes the factor $x_{\mathrm{B}}/(2 - x_{\mathrm{B}})$ that enters in the common form factor decomposition and makes the kinematical coefficients of $\widetilde{\mathcal{E}}$ in the cross section rather small. This redefinition restores also the common "Regge" behavior, i.e., $\overline{\mathcal{E}} \propto x_{\mathrm{B}}^{-\alpha(t)}$ for small x_{B} (see [43]) and simplifies the discussion of the real photon limit for CFFs [17]. However, the common definition is better suited to relate GPDs to form factors.

3.3.1 Maps of asymmetries to CFFs

To determine the sub-CFFs (88) by means of a map (83), we select eight twist-two related asymmetries out of the measured first harmonics, listed in Tab. 2. Thereby, we take the kinematical means from Tab. 1. In any of the possible maps we assume the twist-two dominance hypotheses and we naturally employ for the access of the imaginary parts of the twist-two associated CFFs $\mathcal{F}$ (specified in (88)), the dominant single spin asymmetries in the following sequence

$$\boldsymbol{A}^{\sin} \equiv \begin{pmatrix} A_1 \\ A_2 \\ A_3 \\ A_4 \end{pmatrix} = \begin{pmatrix} A_{\mathrm{LU,I}}^{\sin(1\phi)} \\ A_{\mathrm{UL},+}^{\sin(1\phi)} \\ A_{\mathrm{UT,I}}^{\sin(\varphi)\cos(1\phi)} \\ A_{\mathrm{UT,I}}^{\cos(\varphi)\sin(1\phi)} \end{pmatrix} \quad \Rightarrow \quad \boldsymbol{\mathcal{F}}^{\mathfrak{Im}} = \mathfrak{Im}\begin{pmatrix} \mathcal{H} \\ \widetilde{\mathcal{H}} \\ \mathcal{E} \\ \overline{\mathcal{E}} \end{pmatrix}, \tag{89}$$

see the expressions (26,29,32,35) for asymmetries in terms of CFF combinations (28,31,34,37). The analogous relation for the corresponding even harmonics and the real parts of CFFs reads

$$\boldsymbol{A}^{\cos} \equiv \begin{pmatrix} A_5 \\ A_6 \\ A_7 \\ A_8 \end{pmatrix} = \begin{pmatrix} A_{\mathrm{C}}^{\cos(1\phi)} \\ A_{\mathrm{LL},+}^{\cos(1\phi)} \\ A_{\mathrm{LT,I}}^{\sin(\varphi)\sin(1\phi)} \\ A_{\mathrm{LT,I}}^{\cos(\varphi)\cos(1\phi)} \end{pmatrix} \quad \Rightarrow \quad \boldsymbol{\mathcal{F}}^{\mathfrak{Re}} = \mathfrak{Re}\begin{pmatrix} \mathcal{H} \\ \widetilde{\mathcal{H}} \\ \mathcal{E} \\ \overline{\mathcal{E}} \end{pmatrix}, \tag{90}$$

see (27,30,33,36) and (28,31,34,37). In the following we utilize, however, two different analytic methods for the extraction of the real parts.

First, we consider a linearized map (67), where we take only charge odd asymmetries that arise from the interference of BH and DVCS processes. Thus, we transform the single longitudinally polarized target spin asymmetry $A_{\mathrm{UL},+}^{\sin(1\phi)}$ and the longitudinally double spin-flip asymmetry

$A_{\mathrm{LL},+}^{\cos(1\phi)}$ (both measured only with a positron beam), appearing in the four dimensional vectors (89) and (90), into the charge odd sector. In doing so, we eliminate the interference term in the denominator of these asymmetries by means of the known beam charge asymmetry, i.e. we find from the relation (19):

$$A_{\mathrm{UL,I}}^{\sin(1\phi)} = A_{\mathrm{UL},+}^{\sin(1\phi)}\left[1 + A_{\mathrm{C}}^{\cos(0\phi)} - \frac{1}{2}A_{\mathrm{C}}^{\cos(2\phi)}\right] + \frac{1}{2}A_{\mathrm{UL},+}^{\sin(2\phi)}\left[A_{\mathrm{C}}^{\cos(1\phi)} - A_{\mathrm{C}}^{\cos(3\phi)}\right] + \cdots - A_{\mathrm{UL,DVCS}}^{\sin(1\phi)},$$

$$\approx A_{\mathrm{UL},+}^{\sin(1\phi)}\left[1 + A_{\mathrm{C}}^{\cos(0\phi)}\right], \tag{91}$$

$$A_{\mathrm{LL,I}}^{\cos(1\phi)} = A_{\mathrm{LL},+}^{\cos(1\phi)}\left[1 + A_{\mathrm{C}}^{\cos(0\phi)} + \frac{1}{2}A_{\mathrm{C}}^{\cos(2\phi)}\right] + A_{\mathrm{LL},+}^{\cos(0\phi)}A_{\mathrm{C}}^{\cos(1\phi)} + \frac{1}{2}A_{\mathrm{LL},+}^{\cos(2\phi)}\left[A_{\mathrm{C}}^{\cos(1\phi)} + A_{\mathrm{C}}^{\cos(3\phi)}\right],$$

$$+ \cdots - A_{\mathrm{LL,BH}}^{\cos(1\phi)} - A_{\mathrm{LL,DVCS}}^{\cos(1\phi)},$$

$$\approx A_{\mathrm{LL},+}^{\cos(1\phi)}\left[1 + A_{\mathrm{C}}^{\cos(0\phi)}\right] - A_{\mathrm{LL,BH}}^{\cos(1\phi)}, \tag{92}$$

and we neglect the twist-three related asymmetries $A_{\mathrm{C}}^{\cos(2\phi)}$, $A_{\mathrm{UL},+}^{\sin(2\phi)}$, $A_{\mathrm{LL},+}^{\cos(2\phi)}$, $A_{\mathrm{UL,DVCS}}^{\sin(1\phi)}$, $A_{\mathrm{LL,DVCS}}^{\cos(1\phi)}$, and higher harmonics, indicated by ellipses. Moreover, for the charge odd double longitudinal spin asymmetry, the first harmonic of the BH contribution turns out to be small and can thus be safely subtracted (proton form factor uncertainties are neglected). The imaginary and real parts of the CFFs follow from the solution of two linearized homogenous equation, see (67) with $\boldsymbol{b} = 0$, which we write in the form of the map (83) as

$$\begin{pmatrix}\boldsymbol{\mathcal{F}}^{\mathfrak{Im}}\\ \boldsymbol{\mathcal{F}}^{\mathfrak{Re}}\end{pmatrix} = \frac{1}{N(\boldsymbol{A})}\begin{pmatrix}\boldsymbol{c}_{\mathfrak{Im}} & \boldsymbol{0}_{4\times 4}\\ \boldsymbol{0}_{4\times 4} & \boldsymbol{c}_{\mathfrak{Re}}\end{pmatrix}\cdot\begin{pmatrix}\boldsymbol{A}^{\sin}\\ \boldsymbol{A}^{\cos}\end{pmatrix}. \tag{93}$$

Here $\boldsymbol{0}_{n\times m}$ denotes a n-by-m zero matrix in the 8×8 coefficient matrix $\boldsymbol{c}$, calculated by the inversion of (66), and the first odd and even harmonics

$$\boldsymbol{A}^{\sin} \equiv \begin{pmatrix}A_1\\ A_2\\ A_3\\ A_4\end{pmatrix} = \begin{pmatrix}A_{\mathrm{LU,I}}^{\sin(1\phi)}\\ A_{\mathrm{UL,I}}^{\sin(1\phi)}\\ A_{\mathrm{UT,I}}^{\sin(\varphi)\cos(1\phi)}\\ A_{\mathrm{UT,I}}^{\cos(\varphi)\sin(1\phi)}\end{pmatrix} \quad\text{and}\quad \boldsymbol{A}^{\cos} \equiv \begin{pmatrix}A_5\\ A_6\\ A_7\\ A_8\end{pmatrix} = \begin{pmatrix}A_{\mathrm{C}}^{\cos(1\phi)}\\ A_{\mathrm{LL,I}}^{\cos(1\phi)}\\ A_{\mathrm{LT,I}}^{\sin(\varphi)\sin(1\phi)}\\ A_{\mathrm{LT,I}}^{\cos(\varphi)\cos(1\phi)}\end{pmatrix}, \tag{94}$$

respectively. Consequently, in this linearized map, the cross talk of imaginary and real parts of sub-CFFs arises only via the overall normalization factor, which we analytically determine from the cubic equation (57). The gradient of this linearized sub-CFFs solution can be analytically calculated by means of (70) and the covariance matrix follows from (71,72) and (86).

Unfortunately, the statistics in the double spin-flip asymmetry measurements are rather limited, in particular, for the $A_{\mathrm{LT,I}}^{\sin(\varphi)\sin(1\phi)}$ and $A_{\mathrm{LT,I}}^{\cos(\varphi)\cos(1\phi)}$ harmonics that essentially constrain

the real value of $\mathcal{E}$ and $\overline{\mathcal{E}}$. Hence, we try a more general map (83) where we replace the two longitudinal-transverse double-flip asymmetries in the charge odd sector by the two DVCS-squared related asymmetries $A_{\mathrm{UT,DVCS}}^{\sin(\varphi)\cos(0\phi)}$ and $A_{\mathrm{LL},+}^{\cos(0\phi)}$, which are in general measured with smaller uncertainties, exemplified in Fig. 2. We arrange our eight asymmetries now into three parts,

$$\boldsymbol{A} = \begin{pmatrix} \boldsymbol{A}^{\sin} \\ \boldsymbol{A}^{\cos} \\ \boldsymbol{A}^{\mathrm{DVCS}} \end{pmatrix} \quad \text{with} \quad \boldsymbol{A}^{\cos} \equiv \begin{pmatrix} A_5 \\ A_6 \end{pmatrix} = \begin{pmatrix} A_{\mathrm{C}}^{\cos(1\phi)} \\ A_{\mathrm{LL,I}}^{\cos(1\phi)} \end{pmatrix}, \quad \boldsymbol{A}^{\mathrm{DVCS}} \equiv \begin{pmatrix} A_7 \\ A_8 \end{pmatrix} = \begin{pmatrix} A_{\mathrm{UT,DVCS}}^{\sin(\varphi)\cos(0\phi)} \\ A_{\mathrm{LL},+}^{\cos(0\phi)} \end{pmatrix},$$

$$(95)$$

and $\boldsymbol{A}^{\sin}$ is the same vector as in (94). For the first even harmonics of the charge odd asymmetries $\boldsymbol{A}^{\cos}$ we take here the first two entries of the corresponding four dimensional vector in (94), which are mostly sensitive to the real parts of CFFs $\mathcal{H}$ and $\widetilde{\mathcal{H}}$. Consequently, we split the four-dimensional vector $\boldsymbol{\mathcal{F}}^{\mathfrak{Re}}$ into two two-dimensional vectors,

$$\boldsymbol{\mathcal{F}}^{\mathfrak{Re}} = \begin{pmatrix} \boldsymbol{\mathcal{H}}^{\mathfrak{Re}} \\ \boldsymbol{\mathcal{E}}^{\mathfrak{Re}} \end{pmatrix} \quad \text{with} \quad \boldsymbol{\mathcal{H}}^{\mathfrak{Re}} = \mathfrak{Re}\begin{pmatrix} \mathcal{H} \\ \widetilde{\mathcal{H}} \end{pmatrix} \quad \text{and} \quad \boldsymbol{\mathcal{E}}^{\mathfrak{Re}} = \mathfrak{Re}\begin{pmatrix} \mathcal{E} \\ \overline{\mathcal{E}} \end{pmatrix}. \tag{96}$$

Here, $\boldsymbol{\mathcal{H}}^{\mathfrak{Re}}$ ($= \boldsymbol{\mathcal{F}}$ in the notation of Sect. 3.2.1) is considered as a solution of the inhomogeneous equation (67) and $\boldsymbol{\mathcal{E}}^{\mathfrak{Re}}$ ($= \boldsymbol{\mathcal{G}}$ in the notation of Sect. 3.2.1) governs its inhomogeneous term, i.e.,

$$\boldsymbol{\mathcal{H}}^{\mathfrak{Re}} = \frac{1}{N(\boldsymbol{A})} \boldsymbol{c}_{\mathfrak{Re}} \cdot \boldsymbol{A}^{\cos} - \boldsymbol{c}_{\mathfrak{Re}} \cdot \boldsymbol{b}_{\mathfrak{Re}} \cdot \boldsymbol{\mathcal{E}}^{\mathfrak{Re}}. \tag{97}$$

The transverse single target spin asymmetry in the charge even sector is proportional to the real parts of CFFs $\mathcal{E}$ and $\widetilde{\mathcal{E}}$, see (38), and provides us one linear constraint

$$A_7 \equiv A_{\mathrm{UT,DVCS}}^{\sin(\varphi)\cos(0\phi)} = N(\boldsymbol{A})\, \boldsymbol{c}_{\mathcal{E}}^{\mathsf{T}}(\boldsymbol{A}^{\sin}, \boldsymbol{A}^{\cos}) \cdot \boldsymbol{\mathcal{E}}^{\mathfrak{Re}}, \tag{98}$$

where the $\boldsymbol{c}_{\mathcal{E}}^{\mathsf{T}}$-coefficient depends on the six charge odd asymmetries $\boldsymbol{A}^{\sin}$ and $\boldsymbol{A}^{\cos}$ or sub-CFFs $\boldsymbol{\mathcal{F}}^{\mathfrak{Im}}$ and $\boldsymbol{\mathcal{H}}^{\mathfrak{Re}}$ that are extracted from the set of linear equations. Our system of equations is completed by the measurements of the longitudinal double spin flip asymmetry (47),

$$A_8 \equiv A_{\mathrm{LL},+}^{\cos(0\phi)} = A_{\mathrm{LL,BH}}^{\cos(0\phi)} + A_{\mathrm{LL,I}}^{\cos(0\phi)} + A_{\mathrm{LL,DVCS}}^{\cos(0\phi)}.$$

It contains (in addition to a large BH-squared term) contributions from the polarized interference term and the twist-two DVCS-squared contribution in the numerator. Here we cannot assume that the interference term overwhelms the DVCS-squared term; rather we assume that the two terms enter kinematically on the same level. Hence we have a quadratic constraint for the CFF, which we write as

$$A_8 \equiv A_{\mathrm{LL},+}^{\cos(0\phi)} = N(\boldsymbol{A})\left[a(\boldsymbol{A}^{\sin}, \boldsymbol{A}^{\cos}) + \mathbf{b}^{\mathsf{T}}(\boldsymbol{A}^{\sin}, \boldsymbol{A}^{\cos}) \cdot \boldsymbol{\mathcal{E}}^{\mathfrak{Re}} + \boldsymbol{\mathcal{E}}^{\mathfrak{Re}\mathsf{T}} \cdot \mathbf{c}(\boldsymbol{A}^{\sin}, \boldsymbol{A}^{\cos}) \cdot \boldsymbol{\mathcal{E}}^{\mathfrak{Re}}\right], \quad (99)$$

where all coefficients depend again on the six measurements $\boldsymbol{A}^{\sin}$ and $\boldsymbol{A}^{\cos}$, used previously. The linear constraint (98) together with the quadratical one (99) can be analytically solved, giving us the desired last two sub-CFFs which we write as a matrix equation, too

$$\mathcal{E}^{\Re} = \frac{1}{N(\boldsymbol{A})}\, \boldsymbol{c}_{\mathcal{E}}(\boldsymbol{A}|N(\boldsymbol{A})) \cdot \boldsymbol{A}^{\mathrm{DVCS}}\,, \tag{100}$$

where the 2×2 matrix $\boldsymbol{c}_{\mathcal{E}}(\boldsymbol{A}|N(\boldsymbol{A}))$ is a non-linear function of the eight asymmetries $\boldsymbol{A}$. The final solution can be written as in (83) with a 8×8 coefficient matrix $\boldsymbol{c}(\boldsymbol{A}|N(\boldsymbol{A}))$,

$$\begin{pmatrix} \boldsymbol{\mathcal{F}}^{\Im} \\ \boldsymbol{\mathcal{H}}^{\Re} \\ \boldsymbol{\mathcal{E}}^{\Re} \end{pmatrix} = \frac{1}{N(\boldsymbol{A})} \begin{pmatrix} \boldsymbol{c}_{\Im} & \boldsymbol{0}_{4\times 2} & \boldsymbol{0}_{4\times 2} \\ \boldsymbol{0}_{2\times 4} & \boldsymbol{c}_{\Re} & -\boldsymbol{c}_{\Re} \cdot \mathbf{b}_{\Re} \cdot \boldsymbol{c}_{\mathcal{E}}(\boldsymbol{A}|N(\boldsymbol{A})) \\ \boldsymbol{0}_{2\times 4} & \boldsymbol{0}_{2\times 2} & \boldsymbol{c}_{\mathcal{E}}(\boldsymbol{A}|N(\boldsymbol{A})) \end{pmatrix} \cdot \begin{pmatrix} \boldsymbol{A}^{\sin} \\ \boldsymbol{A}^{\cos} \\ \boldsymbol{A}^{\mathrm{DVCS}} \end{pmatrix}. \tag{101}$$

The normalization $N(\boldsymbol{A})$ is again determined by the consistency equation (57). The gradient of the sub-CFFs solution is calculated by means of (84) and the covariance matrix $\mathrm{cov}(\boldsymbol{\mathcal{F}})$ is calculated from (71), replaced there $\boldsymbol{A}^{\mathcal{I}}$ by $\boldsymbol{A}$, and (86).

A few comments are in order.

It is clear that, within our hypothesis of twist-two dominance, the matrix valued equations (93,101) are solutions of well defined problems. However, in practice we have to deal with the fact that the eigenvalues of $\boldsymbol{c}^{-1}$ (or its inverse $\boldsymbol{c}$) matrix can become very small (big). Obviously, this unpleasant property arises from the fact that in particular the helicity target flip CFFs $\mathcal{E}$ and $\overline{\mathcal{E}}$ are kinematically suppressed in the set of observables.

In addition we have six observables, namely the three lowest harmonics (41,42,43)

$$A_{\mathrm{C}}^{\cos(0\phi)}\,, \quad A_{\mathrm{UT,I}}^{\sin(\varphi)\cos(0\phi)}\,, \quad A_{\mathrm{LT,I}}^{\cos(\varphi)\cos(0\phi)}\,,$$

and three twist-two related asymmetries (38,39,47)

$$A_{\mathrm{UT,DVCS}}^{\sin(\varphi)\cos(0\phi)}\,, \quad A_{\mathrm{LT,BH+DVCS}}^{\cos(\varphi)\cos(0\phi)}\,, \quad A_{\mathrm{LL,+}}^{\cos(0\phi)} \quad \text{for our linearized map (93),}$$

or alternatively the asymmetries (33,36,39)

$$A_{\mathrm{LT,I}}^{\sin(\varphi)\sin(1\phi)}\,, \quad A_{\mathrm{LT,I}}^{\cos(\varphi)\cos(1\phi)}\,, \quad A_{\mathrm{LT,BH+DVCS}}^{\cos(\varphi)\cos(0\phi)} \quad \text{for our map (101),}$$

which are predicted by the extracted twist-two associated CFFs and serve as a consistency check of our extraction procedure. However, we should bear in mind that the three lowest harmonics (41,42,43) may be more strongly contaminated by twist-three related CFFs.

For comparison we will also employ the brute force method, where we solve eight quadratic equations numerically and numerically evaluate the variation of the solution. This allows us to judge the validity of the approximation used to linearize the constraints. Thereby, we can

29

employ the original HERMES data for the first even and odd harmonics (89,90) rather than the transformed ones (94). As for the linearized map, we obviously have six observables for consistency checks available.

Let us now present our results. Within the linearized map we find that the consistency equation for the normalization (57) has two non-trivial real-valued solutions in eleven out of the twelve kinematic bins and the overall asymmetry values, shown in Fig. 2. According to the experimental indications, we pick the solution for the BH regime, where we find for the weighted cross section ratio

$$0.75 \le \frac{\int_{-\pi}^{\pi} d\phi \, w(\phi) d\sigma_{\mathrm{BH}}(\phi)}{\int_{-\pi}^{\pi} d\phi \, w(\phi) \left[d\sigma_{\mathrm{BH}}(\phi) d\sigma_{\mathrm{DVCS}}(\phi) \right]} \le 0.95 \,. \tag{102}$$

The inverse transformation of the sub-CFF solution back to the original asymmetries, where we use the set of non-linear equations, reproduces in general the means and standard errors of the seven asymmetries

$$\left\{ A_{\mathrm{LU,I}}^{\sin(1\phi)}, A_{\mathrm{UL,+}}^{\sin(1\phi)}, A_{\mathrm{UT,I}}^{\sin(\varphi)\cos(1\phi)}, A_{\mathrm{UT,I}}^{\cos(\varphi)\sin(1\phi)}, A_{\mathrm{C}}^{\cos(1\phi)}, A_{\mathrm{LL,+}}^{\cos(0\phi)}, A_{\mathrm{UT,DVCS}}^{\sin(\varphi)\cos(0\phi)} \right\} \,,$$

(the derivatives of which we have used for the map to the sub-CFFs space) in most of the cases on the level of a few percent. We observe in some bins a larger deviation only for $A_{\mathrm{LL,+}}^{\cos(1\phi)}$, which is naturally explained by the fact that we neglected in our linearization procedure the DVCS-squared term, which becomes important if the asymmetry is small. However, also in this case the original data can be considered as well-reproduced. This inverse map is shown for all considered observables in Figs. 8–11, shown in Appendix A, as empty circles. We add that a typical mapping example is presented for the overall asymmetry values in Fig. 2.

A true one-to-one map of random numbers is reached if we use the brute force method, where the start values may be taken from the solution of the linearized map. Moreover, the mean values of the remaining asymmetries, used for the consistency check, are well reproduced on the $\sim 1\sigma$ level, see stars in Figs. 3 and 4.

Let us have a closer look to the problematic bin #3. The linear map (93) yields

$$\mathfrak{Im} \begin{pmatrix} \mathcal{H} \\ \widetilde{\mathcal{H}} \\ \mathcal{E} \\ \overline{\mathcal{E}} \end{pmatrix} = \frac{1}{N(\boldsymbol{A})} \begin{pmatrix} 7.6 \pm 1.2 \\ 1.8 \pm 1.3 \\ -4.5 \pm 6.0 \\ 11.0 \pm 6.1 \end{pmatrix} \quad \text{and} \quad \mathfrak{Re} \begin{pmatrix} \mathcal{H} \\ \widetilde{\mathcal{H}} \\ \mathcal{E} \\ \overline{\mathcal{E}} \end{pmatrix} = \frac{1}{N(\boldsymbol{A})} \begin{pmatrix} 0.4 \pm 2.1 \\ 5.7 \pm 4.1 \\ -28.7 \pm 21.2 \\ -24.8 \pm 22.2 \end{pmatrix} , \tag{103}$$

where the uncertainties are calculated from (72) by neglecting the variation of the normalization. The consistency equation (57) provides us two complex valued solutions $N = 0.5 \pm 0.06 \, i$, where the smallness of the imaginary part tells us that the inconsistency is rather weak. From (103) we

may conclude that the large mean values for $\mathcal{E}^{\mathfrak{Re}}$ and $\overline{\mathcal{E}}^{\mathfrak{Re}}$, which suffer from a large uncertainty, ruin in turn the normalization constraint (57). Indeed, setting one (both) of them to zero allows us to solve the normalization constraint, where $N \sim 0.75\,(0.85)$. There are other possibilities to turn around the normalization inconsistency. In our case the data mapping and/or the linearization procedure imply this inconsistency. Applying the brute-force method to the eight original observables provides the solution:

$$\mathfrak{Im} \begin{pmatrix} \mathcal{H} \\ \widetilde{\mathcal{H}} \\ \mathcal{E} \\ \overline{\mathcal{E}} \end{pmatrix} = \begin{pmatrix} 11.8 \pm 8.9 \\ 2.6 \pm 2.4 \\ -8.1 \pm 13.2 \\ 15.6 \pm 12.7 \end{pmatrix} \quad \text{and} \quad \mathfrak{Re} \begin{pmatrix} \mathcal{H} \\ \widetilde{\mathcal{H}} \\ \mathcal{E} \\ \overline{\mathcal{E}} \end{pmatrix} = \begin{pmatrix} 0.8 \pm 3.6 \\ 6.2 \pm 9.9 \\ -41.9 \pm 52.4 \\ -43.3 \pm 66.6 \end{pmatrix}, \qquad (104)$$

where the errors are propagated as discussed above. From these findings we obtain the relatively small normalization factor[3] $N = 0.64 \pm 0.28$. Substituting this number into (103) shows us that the sub-CFF mean values from the linear map are compatible with those of (104), obtained with the brute-force method. However, in particular, the net error for the sub-CFF $\mathfrak{Im}\,\mathcal{H}$, calculated from the sub-CFF errors (103) and the normalization uncertainty, turns out to be smaller than that in (104).

The resulting CFFs from the linearized (circles) and one-to-one (stars) maps are presented for all twelve bins in Fig. 5. Both maps provide rather similar results, except that the errors for the sub-CFF $\mathfrak{Im}\,\mathcal{H}$ in bins #3, #7, and #11 are approximately two times larger. In these three bins the cross section ratio $N \lesssim 0.7$, calculated from the one-the-one map, is rather small. We conclude that non-linear effects in these circumstances are rather important for the error propagation (see above discussion for bin #3). Clearly, the imaginary part of $\mathcal{H}$ is (as expected) positive, rather large and incompatible with zero. Note that the relatively large errors in bin #5 and #9 are (partially) induced by the fluctuations of $\mathfrak{Im}\,\mathcal{E}$; see for example the analytic expressions for the beam spin (26,28) and the $\cos\phi$ projection (32,34) of the single transverse target spin asymmetries.

All other sub-CFFs can be considered within the uncertainties as compatible with zero. Surprisingly, the imaginary part of $\widetilde{\mathcal{H}}$ possesses even smaller absolute errors than $\mathfrak{Im}\,\mathcal{H}$. Both of these sub-CFFs are contaminated in the first place by proton helicity flip sub-CFFs $\mathfrak{Im}\,\mathcal{E}$ and $\mathfrak{Im}\,\widetilde{\mathcal{E}}$, respectively (see CFF combinations (28) and (31)), which both suffer from larger uncertainties. However, comparing the approximated expressions (26) and (29) for the asymmetries

---

[3]We neglected here correlation of sub-CFF errors otherwise the normalization error increases to 0.48. In turn we also neglect the error correlation in utilizing this normalization error in the linear map (103).

$A_{\text{LU,I}}^{\sin(1\phi)}$ and $A_{\text{UL,+}}^{\sin(1\phi)}$,

$$\frac{A_{\text{LU,I}}^{\sin(1\phi)}}{A_{\text{UL,I}}^{\sin(1\phi)}} \simeq -\frac{y(2-y)}{2-2y+y^2}\frac{\mathfrak{Im}\left[F_1\mathcal{H} - \frac{t}{4M^2}F_2\mathcal{E} + \cdots\right]}{\mathfrak{Im}\left[F_1\widetilde{\mathcal{H}} - \frac{t}{4M^2}F_2\bar{\mathcal{E}} + \cdots\right]},$$

one realizes that the beam spin asymmetry has an additional relative suppression factor,

$$\frac{y(2-y)}{2-2y+y^2} \sim 0.5 \quad \text{with} \quad x_{\text{B}} \sim 0.1 \text{ and } \mathcal{Q}^2 \sim 2.2\,\text{GeV}^2$$

for typical HERMES kinematics. Hence, the larger errors of the polarized longitudinal target spin asymmetry are reduced in the propagation to the sub-CFFs by a factor of two or so. Another reason why the absolute error of $\mathfrak{Im}\,\mathcal{H}$ is larger than of $\mathfrak{Im}\,\widetilde{\mathcal{H}}$ is that the former sub-CFF is more sizeable and so it is also more important for the normalization ratio (57) than the latter. In return, $\mathfrak{Im}\,\mathcal{H}$ suffers from a larger absolute error, see, e.g. the explicit form of the covariance matrix (72) for a linearized map. Note, however, that the twist-two hypothesis may induce here a bias, since we neglected here the twist-three induced $\sin\phi$ harmonic of the DVCS-squared term.

The imaginary parts of the proton helicity flip CFFs $\mathcal{E}$ and $\widetilde{\mathcal{E}}$ are less constrained, partially due to larger errors of the single transversely polarized target spin-flip asymmetries — however, also in part due to their being kinematically suppressed, see (32, 34) and (35,37). Only the real part of the CFF $\mathcal{H}$, also compatible with zero, can be definitely considered as well constrained due to the precise data and since $\mathcal{H}$ dominantly enters in the charge asymmetry (27,28) even without additional y suppression. As one sees, the real parts of the remaining three sub-CFFs are very noisy, in particular, those of the proton helicity flip CFFs. A generic GPD model interpretation of our sub-CFF findings is presented below in Sect. 3.4.

In the alternative map we replace the charge odd asymmetries $A_{\text{LT,I}}^{\sin(\varphi)\sin(1\phi)}$ and $A_{\text{LT,I}}^{\cos(\varphi)\cos(1\phi)}$ by $A_{\text{LL,+}}^{\cos(0\phi)}$ and $A_{\text{UT,DVCS}}^{\sin(\varphi)\cos(0\phi)}$ that contain the DVCS-squared term in the numerator. The normalization is now determined by the non-linear equation, see also (59),

$$N = N(A, N) \quad \text{with} \quad N \in \mathbb{R} \quad \text{and} \quad 0 < N < 1\,,$$

the solution of which yields now four roots. Literally taken, the mapping method is now only applicable in 7 out of 12 bins, namely, in

$$\#1,\ \#2,\ \#4,\ \#9,\ \#10,\ \#11,\ \#12\,,$$

and the overall bin. The failure of the method in bins #3 and #6 is caused by the longitudinal double spin asymmetry measurements $A_{\text{LL,+}}^{\cos(0\phi)}$, which as mentioned above contradicts the assumptions that the BH amplitude overwhelms the DVCS one, see Fig. 3. The failure in bin #8
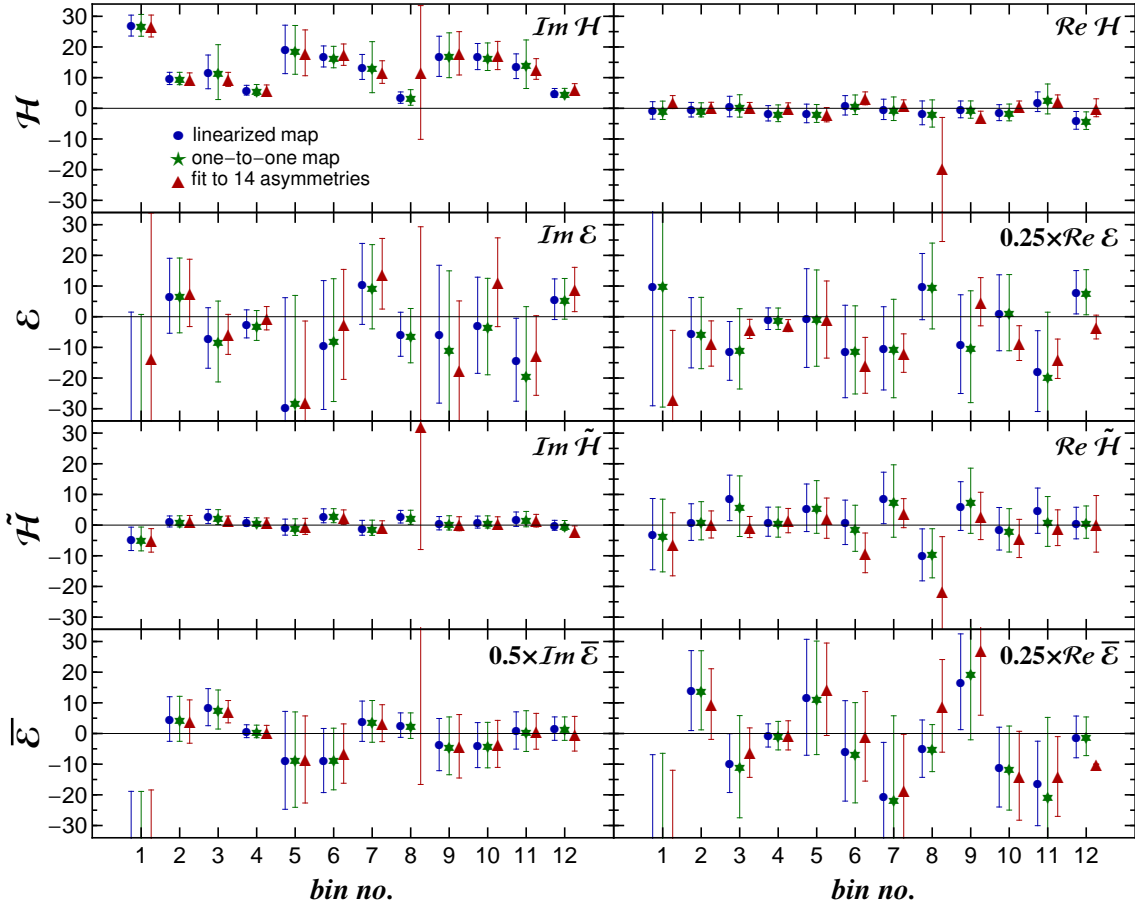
Figure 5: Resulting sub-CFFs from a linearized (circles, shifted to the left) and a one-to-one map (stars) of eight twist-two dominated charge odd asymmetries as well as from a least squares fit (triangles, shifted to the right) to fourteen twist-two related observables for each of 12 HERMES bins.

is related to the large transverse spin asymmetry $A_{\text{UT,DVCS}}^{\sin(\varphi)\cos(0\phi)}$ (see Fig. 4) while the inconsistencies in the mapping method for the bins #5 and #6 are rather weak. Hence, we conclude that, even if the uncertainties of the both replaced charge odd asymmetries are rather large, these observables yield important constraints that ensure the consistency of the mapping method.

3.3.2   Local least squares fits to asymmetries

Let us now employ the method of least squares, where one looks for the minima of the χ^2 function

$$\chi^2(\boldsymbol{\mathcal{F}}) = \left[\hat{\boldsymbol{A}} - \boldsymbol{A}(\boldsymbol{\mathcal{F}})\right]^{\mathsf{T}} \cdot \text{cov}^{-1}(\hat{\boldsymbol{A}}) \cdot \left[\hat{\boldsymbol{A}} - \boldsymbol{A}(\boldsymbol{\mathcal{F}})\right]. \tag{105}$$

Here, the vector $\hat{\boldsymbol{A}}$ contains the measured asymmetries and $\text{cov}^{-1}(\hat{\boldsymbol{A}})$ is the inverse of the covariance matrix. For uncorrelated errors the covariance matrix (86) and its inverse are diagonal

and the χ^2-function (105) reduces to the most common form

$$\chi^2(\mathcal{F}) = \sum_{i=1}^{n} \frac{1}{(\delta A_i)^2} \left[\hat{A}_i - A_i(\mathcal{F}) \right]^2 ,$$

which is well-known. The error propagation is often performed via the Hessian matrix

$$\boldsymbol{H} = \begin{pmatrix} H_{11} & \cdots & H_{1n} \\ \vdots & \vdots & \vdots \\ H_{n1} & \cdots & H_{nn} \end{pmatrix} \quad \text{with} \quad H_{ij} = \frac{1}{2} \frac{\partial^2 \chi^2}{\partial \mathcal{F}_i \partial \mathcal{F}_j} \Big|_{\chi = \chi_{\min}} , \tag{106}$$

where its inverse provides the covariance matrix for the sub-CFFs

$$\text{cov}(\hat{\mathcal{F}}) = \boldsymbol{H}^{-1} . \tag{107}$$

Let us first remind the reader that, instead of finding a one-to-one map of normally distributed random variables with the methods outlined in Sec. 3.2.1 and used in Sect. 3.3.1, one may equivalently utilize the least squares method. Obviously, if a solution (83) exists, written as

$$\hat{\mathcal{F}} = \mathcal{F}(\hat{\boldsymbol{A}}) \quad \text{with} \quad \hat{\boldsymbol{A}} = \boldsymbol{A}(\hat{\mathcal{F}}),$$

the χ^2 function (105) takes exactly the value $\chi^2 = 0$. However, using blindly a "black box" fitting routine to extract the CFF values from DVCS asymmetries, one may find *only one* global minimum with $\chi^2 \approx 0$ due to numerical errors. This solution may be associated to an unphysical root, e.g., in HERMES kinematics it may be associated with a solution where the DVCS cross-section dominates the BH cross-section. Hence, in such "fits" one must search for all $\chi^2 \approx 0$ minima and decide then by means of the cross section ratio (57) which of them is to be considered as the physical one. Alternatively, one may implement the constraint $N(\hat{\mathcal{F}}) > 1/2$ for the BH dominated regime $\left[N(\hat{\mathcal{F}}) < 1/2 \text{ for the DVCS dominated regime} \right]$ or one can constrain the value of a single sub-CFF that is not very well determined by the data. It is easy to realize from (105–107) that, if a one-to-one map exists, the covariance matrix (107) can be written in the form

$$\text{cov}(\mathcal{F}) = \left[\frac{\partial \boldsymbol{A}(\mathcal{F})}{\partial \mathcal{F}} \right]^{-1} \cdot \text{cov}(\boldsymbol{A}) \cdot \left[\frac{\partial \boldsymbol{A}^{\mathsf{T}}(\mathcal{F})}{\partial \mathcal{F}} \right]^{-1} , \tag{108}$$

or by means of the inverse function theorem in the form of (71), constructed from the Jacobian (84). We emphasize that the use of constraints (particularly if the fitted parameter ends on the boundary) may influence the results and so a true one-to-one map cannot be obtained.

We used the equivalence of brute-force and least squares methods, employed for the set of charge odd asymmetries (94), for a numerical cross check between two independent software

tools. Utilizing the popular minimization routine MINUIT [44] in one code and the brute-force method in the other, we obtain (except for bins #3 and #4) the same one-to-one map that is shown in Fig. 5 (stars). In these two bins MINUIT finds global minima in the DVCS dominated regime rather than the BH one, exemplifying that taking here the global minima gives an answer that we consider to be wrong. The small deviation of the total

$$\chi^2 = 2.95 \times 10^{-4} \quad \text{or} \quad \chi^2/n_{\text{d.o.f.}} = \chi^2/(12 \times 8 - 8) = 3.35 \times 10^{-6}$$

value for all 12 bins from zero is here to be considered as a measure of the numerical accuracy rather than reflection of statistical fluctuations.

Obviously, we can employ the least squares method to an ill-posed mapping problem, e.g. as discussed in Sec. 3.3.1 for the alternative map with the set of eight observables (95), where an inconsistency appeared in a few bins. Of course, in such a case the χ^2 value will differ from zero and can be taken as a measure of the inconsistency, which may originate from the statistical fluctuation of means in data.

Moreover, we can use the least squares method also in the case of an overcomplete set of equations. In such a case the χ^2 value of a global minima will also differ from zero. Including the two twist-two associated observables $A_{\text{UT,DVCS}}^{\sin(\varphi)\cos(0\phi)}$ and $A_{\text{LT,BH+DVCS}}^{\cos(\varphi)\cos(0\phi)}$ in the set of the interference term dominated asymmetries (89,90), the total $\chi^2 = 14.3$ value differs now significantly from zero. Note that

$$\chi^2/n_{\text{d.o.f.}} = 14.3/(12 \times 10 - 8) \approx 0.13$$

is naturally a small number and that the χ^2 value in a given bin can be considered as a measure of the size of statistical fluctuations and/or the validity of the utilized twist-two dominance hypothesis. The resulting sub-CFFs are entirely compatible with those from the one-to-one map (not shown).

Extending the twist-two dominance hypotheses also to the lowest asymmetry harmonics, we have 14 observables available and we may consider the twist-two associated sub-CFFs as eight separate independent parameters that we would like to extract. Formulating the extraction problem in such a manner makes closer contact to the work in [25], where all 24 asymmetries that were available at that time were used. In our fit, the total χ^2 value increases to

$$\chi^2 = 67.7 \quad \text{or} \quad \chi^2/n_{\text{d.o.f.}} = 67.7/(12 \times 14 - 8) \approx 0.42 \,,$$

the mean values remain in general stable (see triangles in Fig. 5) except for bin #8 and #12, in which the solution in the DVCS dominated regime is again obtained. For #8 we present the MINUIT outcome and one realizes that the solution in the DVCS dominated regime possesses a very large uncertainty. For bin #12 we used the constraint $|\Re \bar{\mathcal{E}}| < 40$, to find the local

minimum that provides the BH dominated solution. Thereby, the fit ends on a boundary $\mathfrak{Re}\,\bar{\mathcal{E}} = -40$, and, hence, the error propagation for $\mathfrak{Re}\,\bar{\mathcal{E}}$ completely fails—see the corresponding triangle in bin #12 on Fig. 5. Compared to the one-to-one map, the uncertainties naturally decrease and become even smaller than in our linearized map (filled circles). As a consequence of this decrease, one may view now the real part of $\mathcal{E}$ as not any more entirely compatible with zero. In conclusion, extending the twist-two dominance hypothesis also to observables that are potentially more contaminated by the remaining sixteen sub-CFFs and/or the inclusion of constraints may underestimate the errors and can potentially result in an overinterpretation of the resulting sub-CFFs.

Finally, let us compare our findings with those obtained from a regression analysis. Here, one would consider the χ^2 value as a statistical measure and would consider a solution with the value of $\chi^2/\text{d.o.f.} \approx 1$ as optimal. As we have seen, the precision of data and the fact that for any given observable most of the sub-CFFs are kinematically suppressed, presently prevents us from accurately determining all eight sub-CFFs. Although we have already answered the question *'Which sub-CFFs can be extracted with some reliability?'*, in the rest of this section we attempt to address this same question using the method of stepwise regression. Thereby, one first performs eight separate single-sub-CFF fits and sees which sub-CFF alone describes the data best (measured by χ^2 value). Then one proceeds to two-sub-CFF fits, where the best sub-CFF from the first step is combined with each of the seven remaining sub-CFFs and the best-fitting pair of sub-CFFs is retained. This procedure is continued until there is either no improvement in the description of the data or new sub-CFFs are not extracted with any statistical significance.

To make this stepwise procedure more reliable we temporarily remove from consideration the observables $A_{\text{UT,DVCS}}^{\sin(\varphi)\cos(0\phi)}$ and $A_{\text{LT,BH+DVCS}}^{\cos(\varphi)\cos(0\phi)}$ because, for these harmonics, squared combinations of sub-CFFs play a dominant role so a) they cannot be reasonably described in first-step single-sub-CFF fits and b) their inclusion would introduce strong correlations between sub-CFFs in the second and further steps thus potentially introducing bias for some sub-CFFs.

Fitting was performed by standard minimization of the χ^2 function separately in each kinematic bin, using the MINUIT package. As expected, it is $\mathfrak{Im}\,\mathcal{H}$ that gives clearly the best description of all data. The single-sub-CFF fit of $\mathfrak{Im}\,\mathcal{H}$ gives $\chi^2/n_{\text{d.o.f.}} = 198.4/132$, with second best being $\mathfrak{Re}\,\mathcal{H}$ with $\chi^2/n_{\text{d.o.f.}} = 472.7/132$.

In the second step, we have two equally good fits:

- fit of $\mathfrak{Im}\,\mathcal{H}$ and $\mathfrak{Re}\,\mathcal{H}$ with $\chi^2/n_{\text{d.o.f.}} = 102.3/120$, and

- fit of $\mathfrak{Im}\,\mathcal{H}$ and $\mathfrak{Re}\,\mathcal{E}$ with $\chi^2/n_{\text{d.o.f.}} = 103.0/120$.

(Next best being fits to $\mathfrak{Im}\,\mathcal{H}$ and $\mathfrak{Re}\,\widetilde{\mathcal{H}}$ with $\chi^2/n_{\text{d.o.f.}} = 122.4/120$ and to $\mathfrak{Im}\,\mathcal{H}$ and $\mathfrak{Re}\,\widetilde{\mathcal{E}}$ with
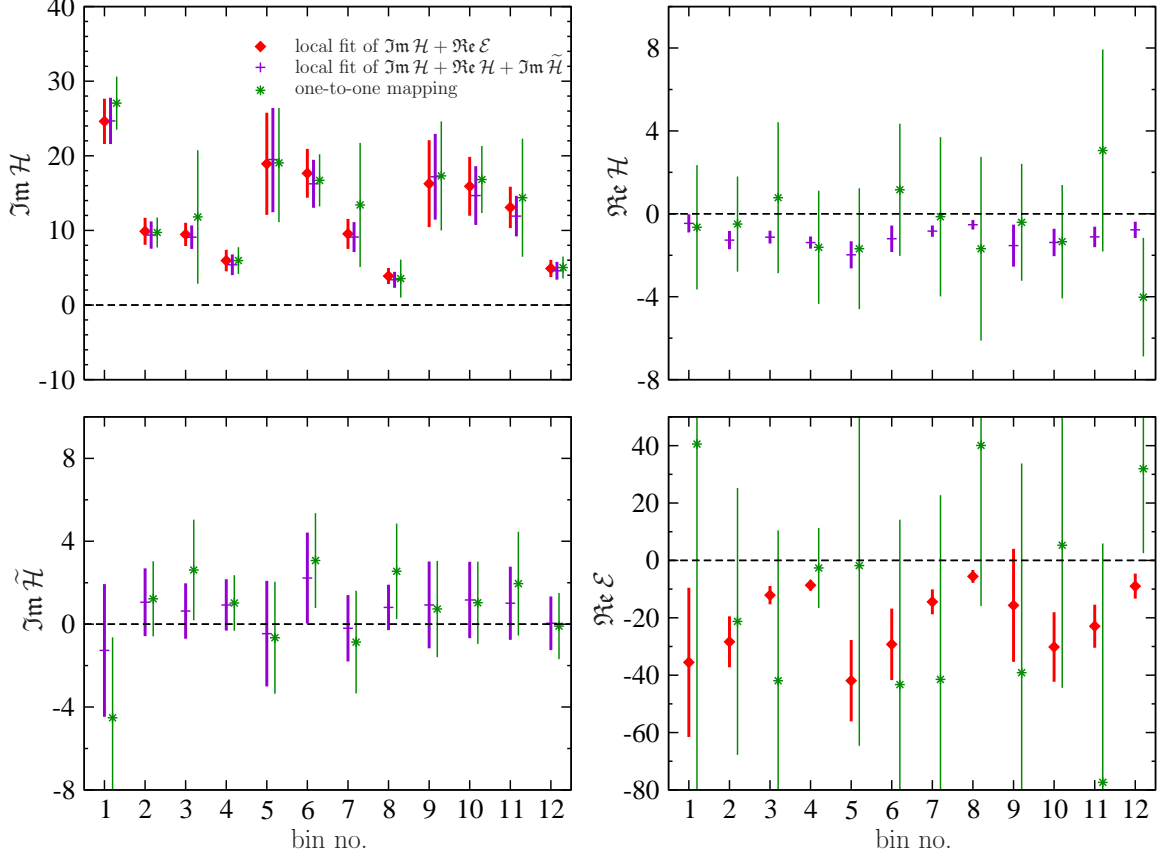
36

Figure 6: Results of least-squares fits in two scenarios with only a small number of CFFs locally fitted to data separately for each of 12 HERMES bins. First, with only $\mathfrak{Im}\,\mathcal{H}$ and $\mathfrak{Re}\,\mathcal{E}$ fitted (red diamonds) and, second, with $\mathfrak{Im}\,\mathcal{H}$, $\mathfrak{Re}\,\mathcal{H}$ and $\mathfrak{Im}\,\widetilde{\mathcal{H}}$ (purple pluses). For comparison, result of one-to-one mapping procedure from section 3.3.1 is also shown (green stars).

$\chi^2/n_{\mathrm{d.o.f.}} = 185.4/120$.) Trying now the third step, for several choices of the third sub-CFF quality of the fits improve somewhat (measured by their p-value) but the values of this third sub-CFF cannot be extracted with any statistical significance. Furthermore, after adding the $A_{\mathrm{UT,DVCS}}^{\sin(\varphi)\cos(0\phi)}$ data, the fits of $\mathfrak{Im}\,\mathcal{H}$ and $\mathfrak{Re}\,\mathcal{E}$ improve much more than the other scenarios due to the dominant contribution of terms involving the $\mathfrak{Im}\,\mathcal{H}\cdot\mathfrak{Re}\,\mathcal{E}$ product to this observable, cf. (38). Thus, as our final results we present two scenarios: one selected by this stepwise regression procedure and another, more in agreement with common expectations, where fits are done with the predetermined set of sub-CFFs $\mathfrak{Im}\,\mathcal{H}$, $\mathfrak{Re}\,\mathcal{H}$ and $\mathfrak{Im}\,\widetilde{\mathcal{H}}$. In both scenarios we now perform fits to the complete set of 14 HERMES observables.

- Scenario 1: Fit of $\mathfrak{Im}\,\mathcal{H}$ and $\mathfrak{Re}\,\mathcal{E}$. $\chi^2/n_{\mathrm{d.o.f.}} = 134.2/144$, when adding χ^2 values for all 12 bins. Fits are bad for bin #3 ($\chi^2/n_{\mathrm{d.o.f.}} = 19.9/12$) and bin #8 ($\chi^2/n_{\mathrm{d.o.f.}} = 21.1/12$). Other bins are fine.

37

- Scenario 2: Fit of $\mathfrak{Im}\,\mathcal{H}$, $\mathfrak{Re}\,\mathcal{H}$ and $\mathfrak{Im}\,\widetilde{\mathcal{H}}$. $\chi^2/n_{\mathrm{d.o.f.}} = 148.8/144$. Bins #3 and #8 again show a bad fit result, with $\chi^2/n_{\mathrm{d.o.f.}} = 21.8/11$ and $\chi^2/n_{\mathrm{d.o.f.}} = 21.1/11$.

We note that, in both scenarios, the fit in bin #8 is fine if the $A_{\mathrm{UT,DVCS}}^{\sin(\varphi)\cos(0\phi)}$ and $A_{\mathrm{LT,BH+DVCS}}^{\cos(\varphi)\cos(0\phi)}$ data points are removed. The resulting sub-CFFs from both scenarios are plotted on Fig. 6 and are compared with the one-to-one map. One realizes that the sub-CFF $\mathfrak{Im}\,\mathcal{H}$ is quite robust and that the real part of CFF $\mathcal{E}$ differs on some 2σ level from zero. The results from the second scenario essentially agree with those in [25], showed there for three selected bins #2, #3, and #4. We add that those results were obtained by means of model-independent least squares fits to *twenty-three* asymmetries. However, most of the asymmetries were not related to twist-two dominated quantities and the sub-CFF parameters were deliberately chosen with reference to GPD model constraints. How successfully fits from our two scenarios (and a global world fit presented in Sect. 3.4) describe particular observables is visible on Figs. 8–11 in Appendix A.

3.4   Uses of HERMES data for model builders and in global fits

Let us discuss the constraints from HERMES DVCS data, presented in terms of CFFs on Fig. 5, for GPD model builders. We consider here the GPD framework in the perturbative leading order (LO) approximation and we can safely restrict ourselves to the qualitative aspects. We adopt and refine here some older discussions, given in Sect. 5.1 of [45] and illuminated with BMK model predictions in Sect. 5.2 there. The imaginary part of CFFs is, in this approximation, given by the GPDs on the cross over line:

$$F(x, x, t, \mu^2 = \mathcal{Q}^2) \overset{\mathrm{LO}}{=} \frac{1}{\pi}\,\mathfrak{Im}\,\mathcal{F}(x_{\mathrm{B}}, t, \mathcal{Q}^2)\Big|_{x_{\mathrm{B}}=\frac{2x}{1+x}}.$$

As known, the valence quark part of GPD H is essentially governed by the asymmetry $A_{\mathrm{LU}}^{\sin(1\phi)}$, which is almost saturated by the valence quark content of the forward PDF, decorated with some t-dependence. On the other hand, rather generic model estimates tell us that sea quark contributions are important in HERMES kinematics, i.e. the partonic decomposition[4] reads

$$\mathfrak{Im}\,\mathcal{H} = \mathfrak{Im}\,\mathcal{H}_{\mathrm{val}} + \mathfrak{Im}\,\mathcal{H}_{\mathrm{sea}} \quad \text{with} \quad \mathfrak{Im}\,\mathcal{H}_{\mathrm{sea}} \sim \mathfrak{Im}\,\mathcal{H}_{\mathrm{val}}. \tag{109}$$

Consequently, the HERMES data, taken in terms of $\mathfrak{Im}\,\mathcal{H}$, require a small skewness effect for GPD H, which is also required for the LO description of HERA collider data. To get an easy handle

---

[4]Our decompositions of CFFs, which are charge even, in valence and sea quark parts contain squared quark charges and the terms *valence* and *sea* are adopted from the common terminology as used in global parton distribution function fits.

on the real part of CFF $\mathcal{H}$, one may use instead of the LO convolution formula a signature-even GPD dispersion relation, see [35, 36, 37, 46] and references therein

$$\mathfrak{Re} \left\{ \begin{matrix} \mathcal{H} \\ \mathcal{E} \end{matrix} \right\} (x_{\mathrm{B}}, t, \mathcal{Q}^2) \stackrel{\mathrm{LO}}{=} \mathrm{PV} \int_0^1 dx \frac{2x}{\xi^2 - x^2} \left\{ \begin{matrix} H \\ E \end{matrix} \right\} (x, x, t, \mu^2 = \mathcal{Q}^2) \pm \mathcal{D}(t, \mathcal{Q}^2) \Big|_{\xi = \frac{x_{\mathrm{B}}}{2 - x_{\mathrm{B}}}} . \quad (110)$$

For HERMES kinematics, we can take for granted that the sign of the resulting real part is determined by the "Regge"-behaviour, inherited from the PDF behavior. Hence, valence quarks provide a large positive real part while sea quarks contribute a negative part and, in addition, there is a subtraction constant that is related to the "D-term" [47]. The HERMES data, taken in the form of $\mathfrak{Re}\,\mathcal{H}$, tell us that the modulus of this quantity is rather small and, hence, we would interpret it as representing a cancelation between the three contributions. Note that the experimental constraint on the subtraction constant depends also on details of the GPD model and it is therefore rather weak.

Going along the same line, we can now discuss the CFF $\widetilde{\mathcal{H}}$. Its real part arises from a signature-odd GPD dispersion relation,

$$\mathfrak{Re} \left\{ \begin{matrix} \widetilde{\mathcal{H}} \\ \widetilde{\mathcal{E}} \end{matrix} \right\} (x_{\mathrm{B}}, t, \mathcal{Q}^2) \stackrel{\mathrm{LO}}{=} \mathrm{PV} \int_0^1 dx \frac{2\xi}{\xi^2 - x^2} \left\{ \begin{matrix} \widetilde{H} \\ \widetilde{E} \end{matrix} \right\} (x, x, t, \mu^2 = \mathcal{Q}^2) \Big|_{\xi = \frac{x_{\mathrm{B}}}{2 - x_{\mathrm{B}}}} , \quad (111)$$

where no subtraction is needed. From phenomenological PDF parameterizations, one expects that the GPD $\widetilde{H}$, taken on the cross-over line and as it enters in the DVCS amplitude, is (much) smaller than GPD H. Hence, one expects that both the real and imaginary parts of CFF $\widetilde{\mathcal{H}}$ are relatively small. This is entirely compatible with HERMES data, which surprisingly provide us also with a rather strong constraint for $\mathfrak{Im}\,\widetilde{\mathcal{H}}$.

A generic discussion can be also given for the CFF $\mathcal{E}$. However, here only form factor information is available. Hence, one would assume that the zero-skewness GPD has a simple functional form in which nodes are absent that arises from Regge and large-x arguments. The normalization of such valence quark GPDs is adopted from the anomalous magnetic moments

$$\kappa_{u_{\mathrm{val}}} = 1.673 \quad \text{and} \quad \kappa_{d_{\mathrm{val}}} = -2.033 \,,$$

taken from the nucleon. A crude approximation of the size of the valence part of $\mathfrak{Im}\,\mathcal{E}$ is obtained if we assume that the same functional form holds for all valence quark contributions,

$$\frac{\mathfrak{Im}\,\mathcal{E}_{\mathrm{val}}}{\mathfrak{Im}\,\mathcal{H}_{\mathrm{val}}} \sim \frac{e_u^2 \kappa_{u_{\mathrm{val}}} + e_d^2 \kappa_{d_{\mathrm{val}}}}{e_u^2 + e_d^2} \sim 1 \quad \Rightarrow \quad \mathfrak{Im}\,\mathcal{E}_{\mathrm{val}} \sim \frac{1}{2} \mathfrak{Im}\,\mathcal{H} \,,$$

where we used (109). However, we should keep in mind that the functional form w.r.t. both the t- and x-dependences may alter our estimates. It is expected that the t- and x-fall off for E GPDs is steeper than for H GPDs [48], i.e. GPD-model-refined estimates would give even

smaller predictions for $\mathfrak{Im}\,\mathcal{E}_{\rm val}$. Considering the CFF data in Fig. 5, one realizes that the noise of $\mathfrak{Im}\,\mathcal{E}$ is of the order of the means of $\mathfrak{Im}\,\mathcal{H}$. Hence, contrary to GPD-model-based claims, e.g. that HERMES data provide a constrain on the quark orbital angular momentum decomposition [13] or the suggestion that negative sea quark contributions to $\mathfrak{Im}\,\mathcal{E}$ are favored [49], our generic arguments tell us that a partonic interpretation of HERMES data in this specific case is entirely biased by model assumptions. Let us add that the dispersion relation (110) that we used for an estimate of $\mathfrak{Re}\,\mathcal{E}$, together with the standard model assumptions, tells us that the large negative $\mathfrak{Re}\,\mathcal{E}$ scenario that we obtained from the regression method is difficult to understand from the GPD model perspective (positive subtraction constant for negative D-term, positive contribution for valence quarks, and positive contribution for negative sea quarks).

To complete our short examination of the CFF data, we mention that the CFF $\widetilde{\mathcal{E}}$ should contain a pion pole contribution that should be large at small $-t$ [50, 51]. Sometimes, GPD model builders believe that this is the most important contribution and neglect for that reason the imaginary part. If one wishes, one can see sizeable and negative $\widetilde{\mathcal{E}}$ sub-CFFs at small $-t$ — see the first bin in Fig. 5 where the significance for the imaginary part is even more pronounced than for the real part. This clearly contradicts the common GPD model assertion. However, since these data are very noisy, a definite conclusion cannot be drawn and we consider the CFF $\widetilde{\mathcal{E}}$ as essentially unconstrained from HERMES DVCS data.

For comparison purposes, we also performed one global model fit to the world DVCS off-the-proton data with a version of the hybrid model used in [38] that we initially used to access the GPD H from unpolarized proton DVCS data. The hybrid model comprises a full GPD model in the flavor singlet sector (dominated at small $x_{\rm B}$ by sea quark and gluon contributions), while in the flavor non-singlet (or valence quark) sector dispersion relations are used and, hence, only the GPDs on the cross-over line are needed. Keeping in mind that, apart from HERMES, no other experiment with a proton target could provide information on the full separation of the various CFF contributions, we neglect in our fit the $\mathfrak{Im}\,\mathcal{E}$ and $\mathfrak{Im}\,\widetilde{\mathcal{E}}$ contributions, which are compatible with zero for HERMES kinematics. However we do include $\mathfrak{Re}\,\mathcal{E}$ and $\mathfrak{Re}\,\widetilde{\mathcal{E}}$, which are related to subtraction constants in the dispersion relation (110) and in the oversubtracted analog of (111), respectively. The reason for doing so is that HALL A unpolarized cross section measurements [52] indicate a rather large unpolarized DVCS cross section, which suggest that the DVCS amplitude contains a large real part. In our hybrid model, the contributions of sea quarks and gluons are modelled using conformal moments of GPDs $H^{\rm sea}$ and $H^{\rm G}$, respectively, and LO QCD evolution is taken into account, while the contributions of valence quarks are described by directly modelling $\mathfrak{Im}\,\mathcal{H}$ and $\mathfrak{Im}\,\widetilde{\mathcal{H}}$ and using dispersion relations to obtain $\mathfrak{Re}\,\mathcal{H}$ and $\mathfrak{Re}\,\widetilde{\mathcal{H}}$ (and evolution is neglected). Details of the model are given in ref. [38], to which we

refer the interested reader.

In particular, we used the following data sets:

- The HERMES combined data on $A_{\mathrm{LU,I}}^{\sin(1\phi)}$, $A_{\mathrm{C}}^{\cos(0\phi)}$ and $A_{\mathrm{C}}^{\cos(1\phi)}$ [22]; on $A_{\mathrm{UL},+}^{\sin(1\phi)}$ and $A_{\mathrm{LL},+}^{\cos(0\phi)}$ [21]; and on $A_{\mathrm{UT,I}}^{\sin(\varphi)\cos(1\phi)}$ [13]. To work with statistically independent data we considered only the projection of the data along the $-t$ axis, i.e. just the first third of the published 18 [22] or 12 [13, 21] kinematic bins. This gives $3 \times 6 + 2 \times 4 + 4 = 30$ data points.

- The first $(\sin\phi)$ harmonics of the CLAS data on a) the beam spin asymmetry with an unpolarized target [53], where we used only data with $\mathcal{Q}^2 > 2\,\mathrm{GeV}$ (4 points), and b) the longitudinal target spin asymmetry with a polarized target [54] (6 points).

- Fourier transforms of the Hall A measurements of beam spin difference (12 points) and beam spin sum (8 points) [52], where cross-sections were weighted with the inverse product of the Bethe-Heitler propagators.

- Measurements by the H1 collaboration of

  - The DVCS cross section differential in t, [55], Table 1, 1996-1997 data (4 points) and 1999-2000 data (4 points).
  - The DVCS cross section differential in t, [56], Table 3a, (12 points).

- Measurements by the ZEUS collaboration of

  - The DVCS cross section differential in t, [57], Table 1, only $\mathcal{Q}^2 > 4\,\mathrm{GeV}^2$ points (5 points).
  - The total DVCS cross section, [57], Table 4 (4 points).
  - The total DVCS cross section, [58], Table 1 (6 points).

In total, we have 95 data points. Fitted to these points was a version of the model used in [38]. Here we only describe differences, and list the free fitting parameters. The first difference is that, beside leading partial wave in SO(3) expansion of conformal moments of GPDs H^{sea} and H^{G} (the normalization of which is fixed by DIS F_2 data, and residual t-dependence of H^{sea} being determined by free dipole mass parameter M^{sea}) and subleading partial wave with relative strength parameters s_2^{sea} and s_2^{G}, we take here into account also the third partial wave with two new strength parameters s_4^{sea} and s_4^{G}. The second difference to [38] is that $\mathfrak{Re}\,\widetilde{\mathcal{E}}$ is here modelled by a shape suggested by the pion pole contribution, but with normalization r_π and additional t-slope dipole mass M_π as two additional free parameters. Together with parameters M^{val}, r^{val}, and b^{val} parametrizing $\mathfrak{Im}\,\mathcal{H}$, C and M_C parametrizing subtraction constant[5], and $\widetilde{M}^{\mathrm{val}}$, $\widetilde{r}^{\mathrm{val}}$,

---

[5]Note that the subtraction constant here is given by $-\mathcal{D}$, appearing in (110).

M^{val}	r^{val}	b^{val}	C	M_C	$\tilde{M}^{\text{val}}$	$\tilde{r}^{\text{val}}$	$\tilde{b}^{\text{val}}$	r_π	M_π
0.95	1.12	0.40	1.00	2.08	3.52	1.30	0.40	3.84	4.00

$(M^{\text{sea}})^2$	s_2^{sea}	s_4^{sea}	s_2^{G}	s_4^{G}
0.46	0.31	-0.14	-2.77	0.94

Table 3: Valence (top) and sea quark (bottom) related hybrid model parameters, extracted from the global DVCS fit *KMM12*.

and $\tilde{b}^{\text{val}}$ parametrizing $\mathfrak{Im}\,\widetilde{\mathcal{H}}$ in the same way as in [38], this brings the number of parameters to a total of 15. The fit of this model to all of the above data results in $\chi^2/n_{\text{d.o.f.}} = 124.1/80$, which is strictly speaking not a good fit, but it is acceptable for a global fit to data coming from such a variety of experiments and observables. Parameters of the fitted model are given in Tab. 3. and the values resulting from this global fit for the 10 HERMES observables used for local fits in previous sections are given by solid lines on Figs. 8–11 in Appendix A.

We now finally considerthe possible tension between our simple GPD model fit and the data. As one can see in Fig. 8, our fit reasonably describes the beam spin and beam charge asymmetries, but shows a slight tendency for the mean values to slightly overshoot the data values. This, as discussed above, is related to the problem of overshooting the beam spin asymmetry measurements, taken from events selected by the missing mass technique, with GPD models which employ a leading order description that have skewness ratios $r \gtrsim 1$. The tension that appears in the lowest x_{B} and $\mathcal{Q}^2$ bin for the first harmonic of the beam charge asymmetry may be related to a technicality; namely, our input scale for evolution is chosen to be $4\,\text{GeV}^2$ and backwards evolution to $\mathcal{Q}^2 \lesssim 1.5\,\text{GeV}^2$ in the flavor singlet sector is a delicate procedure that is rather sensitive to the initial conditions. The dominant longitudinal proton spin-flip asymmetry is also overvalued by the model, see Fig. 9, which just reflects the fact that the description of unpolarized HALL A cross section measurements requires a large real part in the DVCS amplitude which is partially also obtained via a GPD dispersion relation from the imaginary part of CFF $\widetilde{\mathcal{H}}$. Such a parametrization, which is effective for unpolarized DVCS measurements, is clearly disfavored if longitudinal proton spin-flip asymmetry data are included. The transverse proton spin-flip asymmetries, shown in Fig. 10 are well described by our $\mathfrak{Im}\,\mathcal{E} = \mathfrak{Im}\,\widetilde{\mathcal{E}} = 0$ models, within the large experimental uncertainties. Mostly, this is also the case for the transverse proton spin-flip asymmetries, presented in Fig. 11. As an exception on might view $A_{\text{LTI}}^{\cos(\varphi)\cos(1\phi)}$, given in (36), where one may see some hint that the sign of the real part of $\widetilde{\mathcal{E}}$, adopted from the pion pole, contradicts data. Let us emphasize that the basic modeling of $\widetilde{\mathcal{E}}$ in terms of pion pole contribution is oversimplified and already contradicts the GPD interpretation

of π^+ electroproduction data in the collinear framework [43, 59].

Compared to previous good DVCS world data fits to data from an unpolarized proton, having $\chi^2/\text{d.o.f.} \approx 1$, we may interpret our findings here as a slight tension between a very simple model and fixed target data. One may argue that this tension is induced by the attempt to explain the unpolarized photon electroproduction cross section data from JLab Hall A by means of the common four twist-two GPDs, which have a oversimplified functional form. A definite conclusion cannot be given, however, since one may use more intricate parameterizations of these four twist-two GPDs, or use an improved framework by inclusion of perturbative corrections, certain twist-three [60, 61, 62] and twist-four contributions [63, 64], or extend the number of GPDs and thus CFFs. Certainly, there are also experimental uncertainties related to the issue of exclusivity, in particular the potential inclusion of events including a Δ-resonance within the experimental data set. We emphasize, however, that the inclusion of polarized proton data does not contradict the conclusion that GPD H plays the dominant role in the description of present DVCS data.

4   Summary and outlook

In this article we analyzed, by means of mapping and regression methods, the final set of DVCS off-the-proton data from the HERMES collaboration extracted using a missing-mass event selection method. Thereby, we still utilized the twist-two dominance hypothesis and, thus, we restricted ourselves to an overcomplete set of *fourteen* asymmetries. We showed that the HERMES collaboration provided an experimental proof of principle that, with an (almost) complete measurement of *eight* first harmonic asymmetries in the charge-odd sector, all four twist-two associated CFFs can be accessed in a BH dominated regime. In the remaining *six* zero harmonic asymmetries the CFFs are kinematically suppressed and we used them to check the twist-two dominance hypothesis or, alternatively, employed them to access twist-two associated CFFs. Higher harmonics, in the first place related by the remaining set of *eight* CFFs, were not considered.

Apart from restricting ourselves to the twist-two sector, our analysis is rather general. We tested different methods to access CFFs: mapping, local regression analysis, and model fits. In any CFF (or GPD model) extraction procedure from a set of asymmetries, one *must* bear in mind that separate solutions may exist for the BH dominated and the DVCS dominated regimes. Based on experimental evidence and model expectations, we took in our analysis the BH dominated solution. A one-to-one map of asymmetries to the space of CFFs can be either found by picking up the appropriate roots of a non-linear equation system (in our case eight equations that can
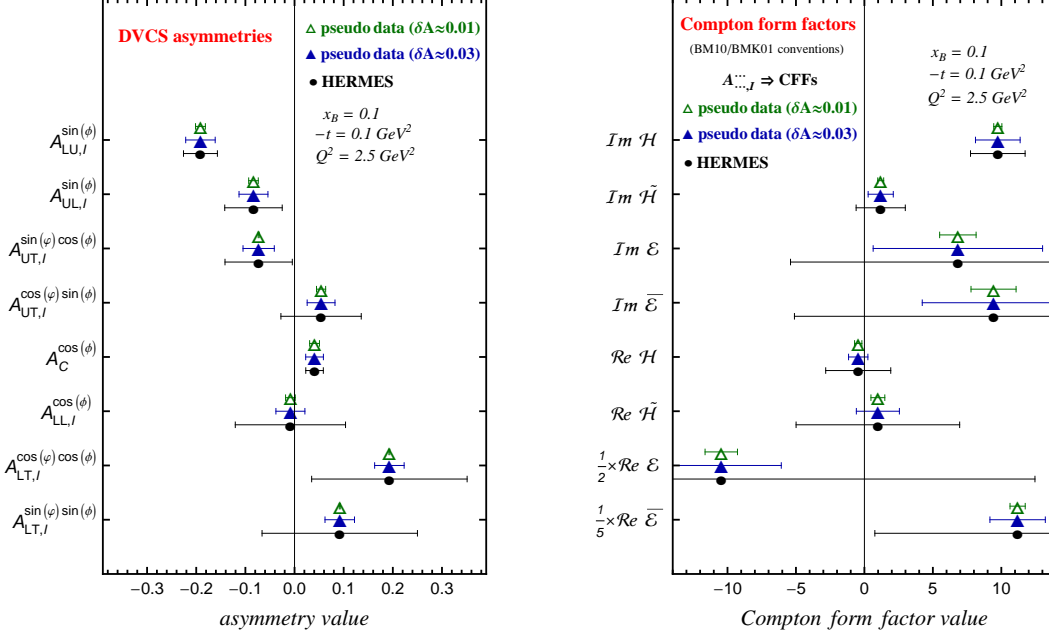
Figure 7: Left: Two projections with total errors $0.01 \lesssim \delta A \lesssim 0.03$ (filled triangles) and $\delta A \approx 0.01$ (empty triangles) of charge odd asymmetries (left) for $x_{\mathrm{B}} = 0.1$, $t = -0.1\,\mathrm{GeV}^2$, and $\mathcal{Q}^2 = 2.5\,\mathrm{GeV}^2$ are compared with HERMES measurements in bin #2 (solid circles). Right: the resulting CFFs from a one-to-one map, based on the twist-two dominance hypothesis.

be linearized) or, equivalently, by the least squares method. However, numerical noise in a blind "fitting" technique can provide an unphysical solution. Constraining the value of CFFs to force a "black box" fitting routine to provide the physical solution, a rather popular method, may have the disadvantage that a true one-to-one map cannot be obtained. The inclusion of more (twist-two related and unrelated) asymmetries in a fitting procedure will increase the noise and the physical solution is not necessarily obtained from the global minimum.

In a one-to-one map of interference dominated, mostly charge-odd asymmetries, it turns out that only the imaginary part of CFF $\mathcal{H}$ is not compatible with zero, and all other seven sub-CFFs can be considered as compatible with zero. Surprisingly, it turns also out that the best constrained quantity is the imaginary part of CFF $\widetilde{\mathcal{H}}$, followed by the real part and imaginary parts of $\mathcal{H}$, and to a much lesser extent also by the imaginary part of CFF $\mathcal{E}$. The remaining four sub-CFFs are very poorly constrained. One may be tempted to consider the extraction of CFFs as a regression problem, and thus use selection criteria for filtering out the noise. As expected, in this approach it turns out that $\mathfrak{Im}\,\mathcal{H}$ is a robust quantity, the method does not necessarily yield a unique solution. We present two solutions: one obtained by the strict use of selection criteria and the other a more hand-picked solution informed by standard GPD model considerations.

44

The first one suggests that the negative real part of CFF $\mathcal{E}$ can be considered as large and the second solution suggests that one may consider the real part of CFF $\widetilde{\mathcal{H}}$ as negative and the imaginary part of $\widetilde{\mathcal{H}}$ as positive. Certainly, from the GPD model point of view one would give the hand-picked standard solution preference. However, we emphasize that our one-to-one map only shows that this well constrained quantity $\mathfrak{Im}\,\widetilde{\mathcal{H}}$ is small and does not allow a further partonic interpretation, e.g., extraction of any t-dependence. A rather analogous situation appears for the imaginary part of CFF $\mathcal{E}$ — its magnitude is only loosely constrained by the data. The relation of GPD E to the spin sum rule inspires both experimentalists and theoreticians to make definite GPD model statements that certainly cannot, at present, be justified by simply describing experimental DVCS data with a given model. This we have illuminated in our global GPD model fit example where the GPD E (in the standard double distribution representation) has been set to zero, giving us the perhaps best (however, not perfect) DVCS world data description that is presently available.

Let us illustrate that with the HERMES experiment, switched off 2007, our knowledge about CFFs could have been much better. Supposing that the longitudinally polarized proton asymmetries $A_{\mathrm{UL,I}}$ and $A_{\mathrm{LL,I}}$ would have been measured in the charge-odd sector with the same statistics and slightly better systematics than the existing data taken with positron beam, the proton helicity conserved CFFs $\mathcal{H}$ and $\widetilde{\mathcal{H}}$ could have been accessed with roughly the same accuracy. Alternatively, a decrease of the large statistical uncertainties for the $A_{\mathrm{LT,I}}$ quantities to a typical value of other HERMES asymmetries would have drastically improved the constraints for the real parts of proton helicity flip CFFs $\mathcal{E}$ and $\widetilde{\mathcal{E}}$ (note, however, that these CFFs naturally suffer from a larger uncertainty). The effect of a decrease in the uncertainties that would be feasible at a fixed target experiment such as HERMES is illustrated by the filled triangles in Fig. 7, where we naively assumed for all polarized charge odd asymmetries a $\delta A \approx 0.03$ error (statistical and systematic uncertainties are added in quadrature).

The HERMES collaboration provided a total set of *thirty-four* asymmetries that includes an (almost) complete measurement of the second harmonic asymmetries in the charge odd sector, which are primarily associated with *four* twist-three and *four* twist-two related CFFs. In principle, *twenty-four* asymmetries can be utilized in a one-to-one map, which leaves us ten asymmetries for a consistency check. Due to kinematic suppressions and noise it is expected that access to the *eight* twist-tree and transversity associated CFFs is not achievable; however one may hope for a test of whether our (and other) results are robust in an unbiased map, i.e. where one drops the twist-two dominance hypothesis. Before one undertakes such an attempt, several improvements and technicalities should be taken into account, which are partially also needed on more general grounds:

- A physically motivated parametrization of the DVCS tensor in terms of *twelve* CFFs.

- A code which relates the set of *twelve* well defined CFFs to observables in an *exact* manner, perhaps for different conventions.

- The (small) differences between proton polarization vector, defined in the lab frame, and those in the rotated frame, see Fig. 1, should be taken into account, at least from the principled point of view.

- It would be desirable that the covariance matrix for experimental measurements would be available for each given kinematical bin.

Let us add to the first two points that various codes are presently used that relate (twist-two associated) CFFs (in most cases understood as quantities that are expressed by conventionally defined GPDs) that are based on different conventions and approximations. At present numerical differences do not matter, nevertheless, it is not desirable to proceed in this manner to the next generation of DVCS experiments. The remaining obstacles can be overcome by means of the parameterization for the virtual Compton scattering tensor and the analytic cross section results that are presented in [17].

In planned DVCS experiments at JLAB@12GeV, having an electron beam and fixed proton target, it is expected that experimental uncertainties will become much smaller, as already demonstrated by the HALL A collaboration in measurements of DVCS cross sections. Altogether in such an experimental set up one can measure *eight* (*seven*) azimuthal angular dependent cross section combinations (asymmetries), compared to *sixteen* (*fifteen*) for both charges of electrons. Having precise cross section measurements, one can form, at least in principle, 4×4 even and 4×3 odd harmonics, giving us *twenty-four* independent and four dependent (constant term) observables. Hence, one may have a handle on the CFF separation via a harmonic analysis [14]. Qualitatively or semi-quantitatively, one may also employ Rosenbluth separation to address the three separate parts of the photon electroproduction cross section. To which extent this separation is feasible requires detailed studies, where, unfortunately, the results will depend on assumptions. However, the possibility of obtaining any unbiased extraction of CFFs cannot be clearly stated at present. Certainly, a clean separation of the charge odd (interference term) and charge even part (sum of BH and DVCS cross sections) requires a high-luminosity positron beam, too. Supposing that in a (next-to-) next generation of lepton-proton scattering experiments both kinds of electrons are available and the total experimental uncertainties for all asymmetry (or, better, cross section difference) measurements are three times smaller than those of the beam-spin asymmetry measurements at HERMES, see empty triangles on Fig. 7, we may expect that

the CFF $\mathcal{E}$ can be accessed in the BH-dominated DVCS regime with an accuracy that is presently available for CFF $\mathcal{H}$.

Acknowledgements
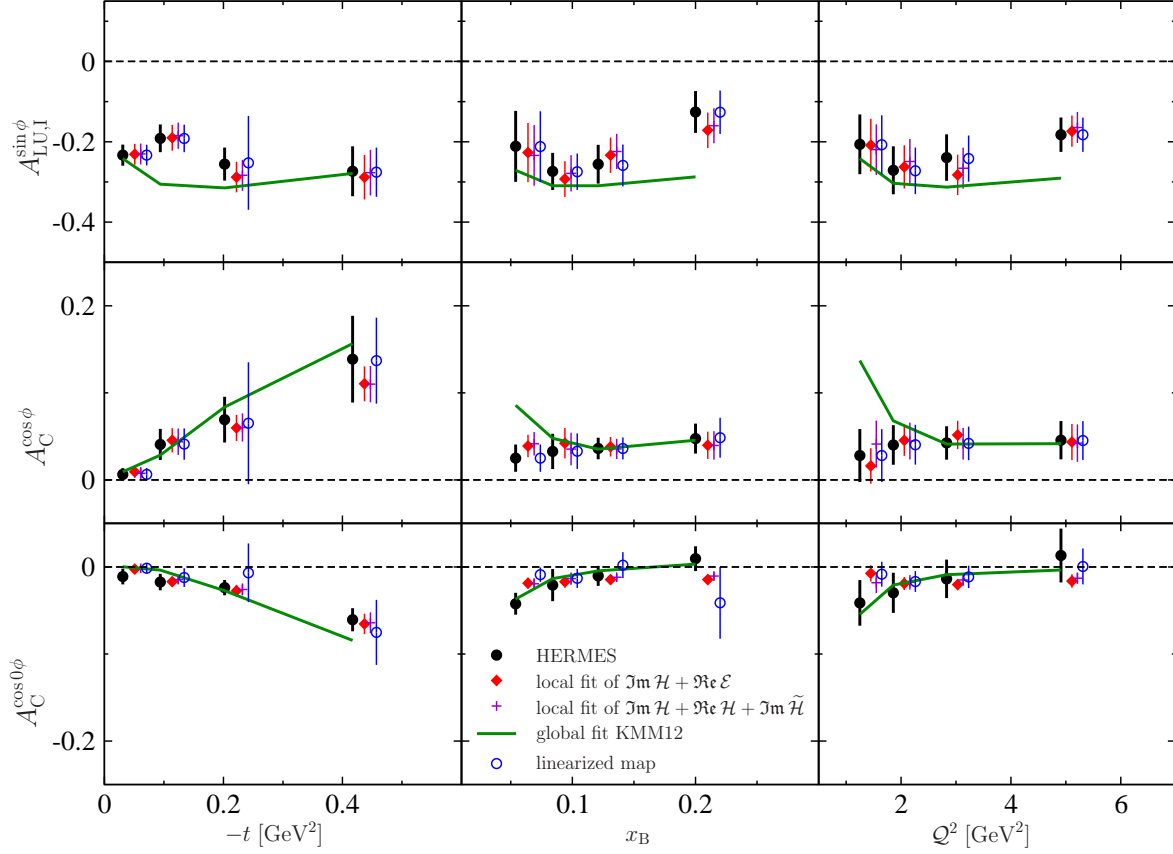
A Visualization of HERMES data descriptions

Figure 8: Fits to harmonics of asymmetries of scattering on an *unpolarized* target. Black dots are HERMES data with systematic errors added in quadrature. Local fits in two different scenarios are shown as red diamonds (fit to $\mathfrak{Im}\,\mathcal{H}$ and $\mathfrak{Re}\,\mathcal{E}$) and blue pluses (fit to $\mathfrak{Im}\,\mathcal{H}$, $\mathfrak{Re}\,\mathcal{H}$, and $\mathfrak{Im}\,\widetilde{\mathcal{H}}$), slightly displaced to the right for legibility. For comparison, we also show the result of a global fit to world DVCS data as a green solid line.
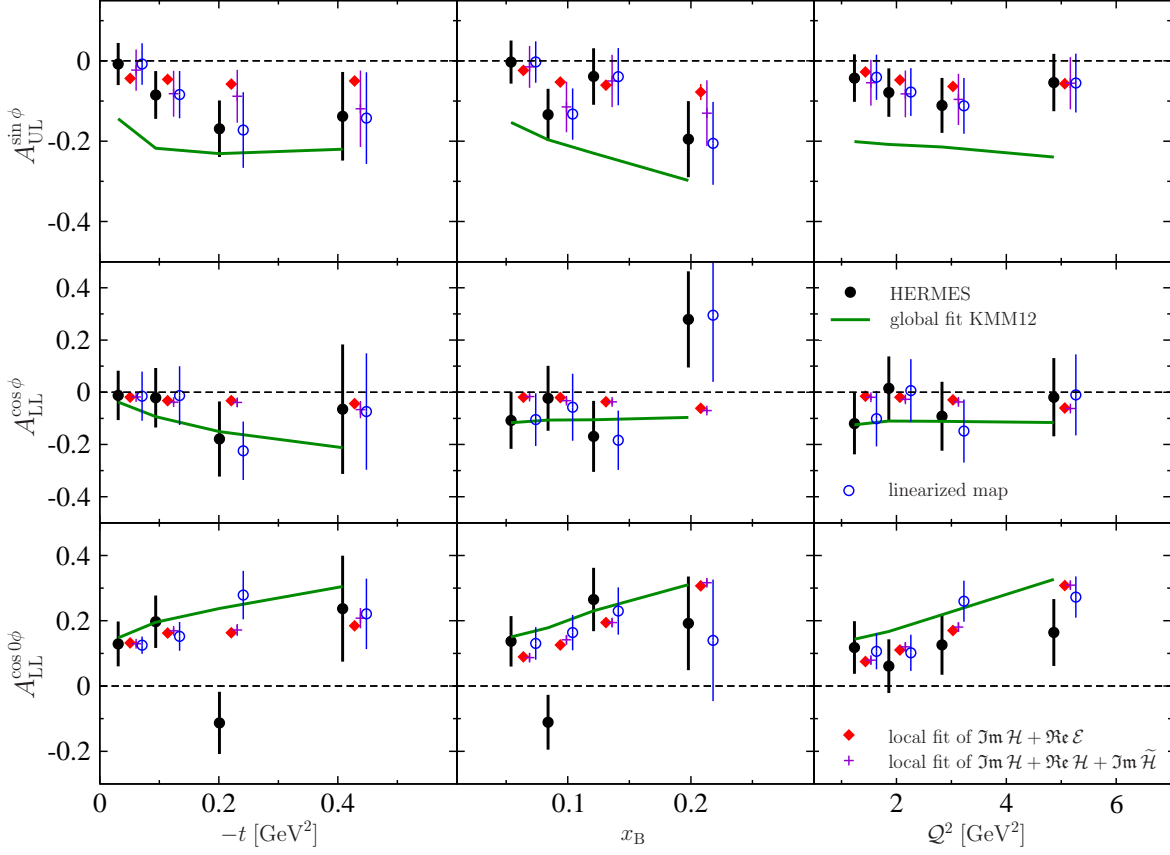
Figure 9: Fits to *longitudinally polarized* target asymmetry harmonics. Legend is as for Fig. 8
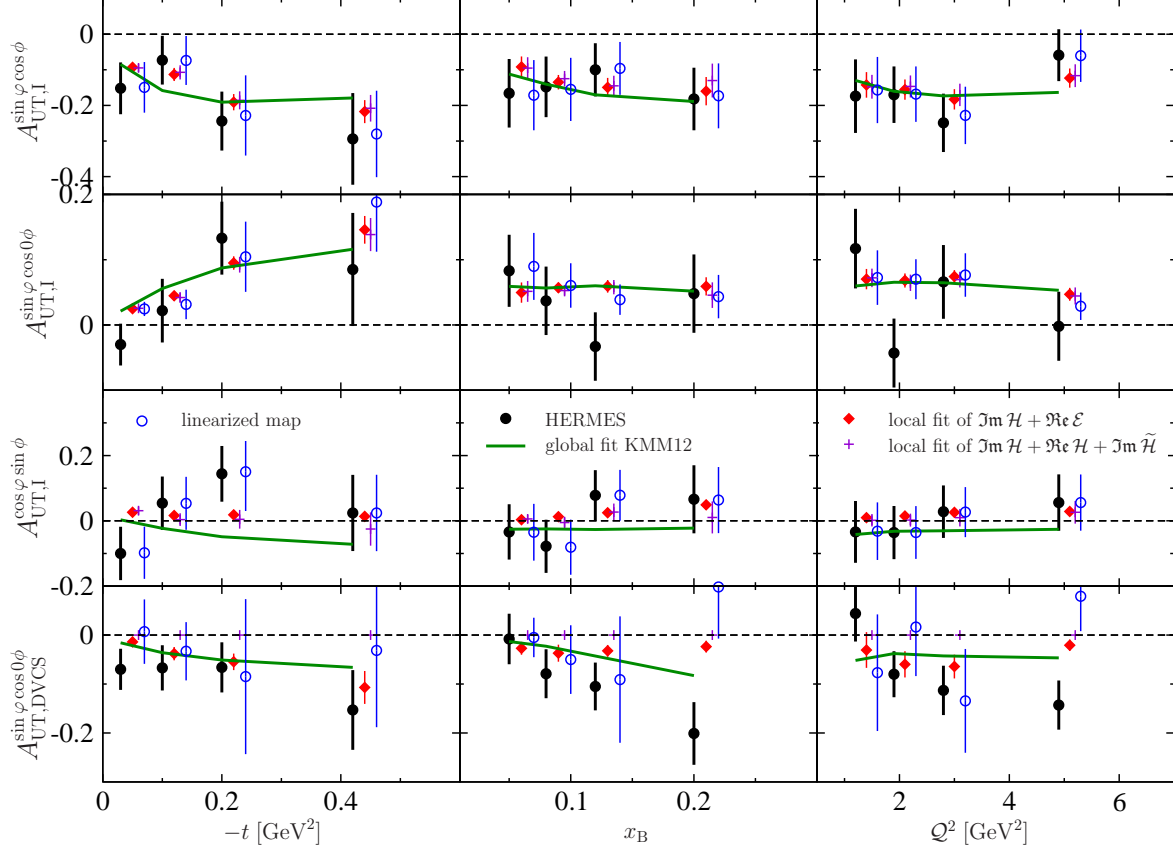
Figure 10: Fits to *transversely polarized* target asymmetry harmonics. Legend is as for Fig. 8
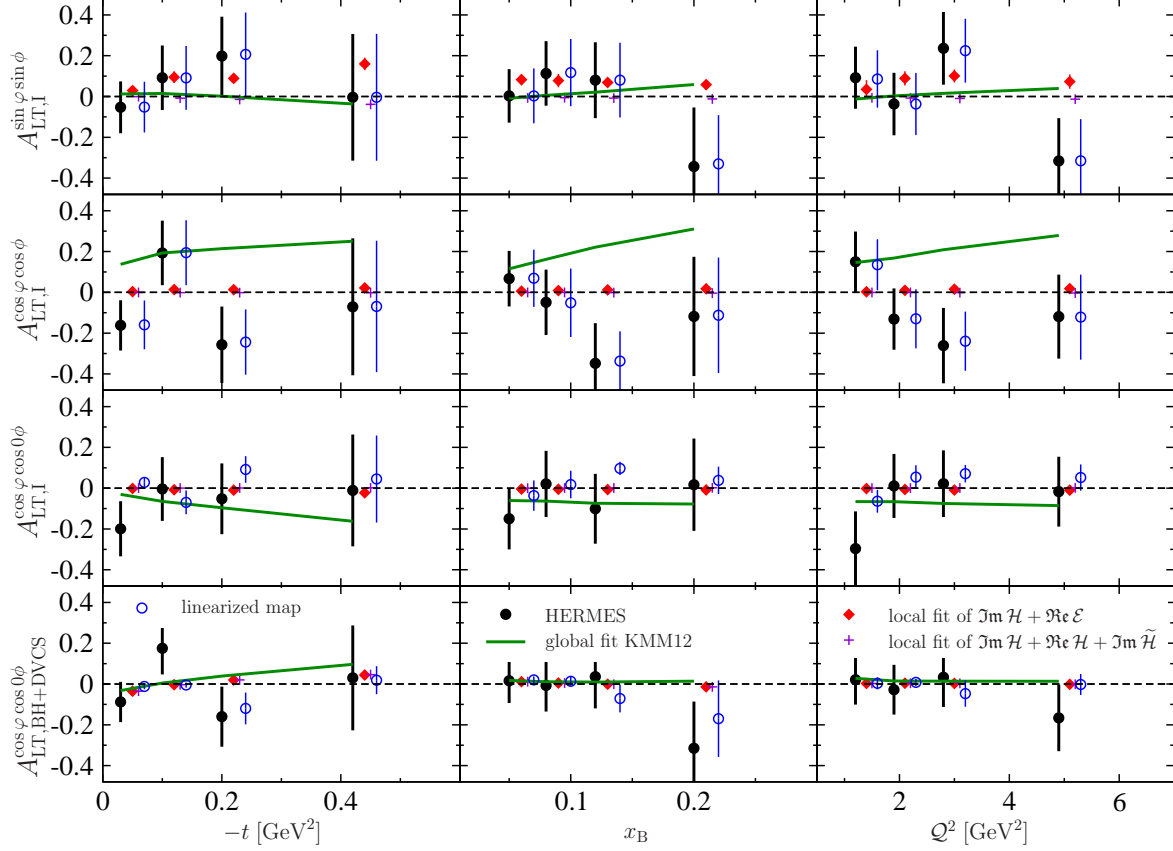
Figure 11: Fits to asymmetry harmonics of *polarized* electron/positron beam scattering on a *transversally polarized* target. Legend is as for Fig. 8

References

[1] *Compton A. H.*, Phys.Rev. **21**, 1923, 483.

[2] *Guichon P. A., Liu G., Thomas A. W.*, Nucl.Phys. **A591**, 1995, 606, nucl-th/9605031.

[3] *Müller D., Robaschik D., Geyer B., Dittes F.-M., Hořejši J.*, Fortschr. Phys. **42**, 1994, 101, hep-ph/9812448.

[4] *Radyushkin A. V.*, Phys. Lett. **B380**, 1996, 417, hep-ph/9604317.

[5] *Ji X.*, Phys. Rev. **D55**, 1997, 7114, hep-ph/9609381.

[6] *Ji X.*, Phys. Rev. Lett. **78**, 1997, 610, hep-ph/9603249.

[7] *M. Burkardt*, Phys. Rev. **D62**, 2000, 071503, hep-ph/0005108, Erratum-ibid.D66, 2002, 119903.

[8] *Ralston J. P., Pire B.*, Phys. Rev. **D66**, 2002, 111501, hep-ph/0110075.

[9] ZEUS, *Saull P.*, "Prompt photon production and observation of deeply virtual compton scattering", 2000, hep-ex/0003030.

[10] HERMES, *Amarian M.* , AIP Conf. Proc. 570, pp. 428-432 DESY-HERMES-00-47

[11] HERMES, *Airapetian A., et al.*, Phys. Rev. Lett. **87**, 2001, 182001, hep-ex/0106068.

[12] CLAS, *Stepanyan S., et al.*, Phys. Rev. Lett. **87**, 2001, 182002, hep-ex/0107043.

[13] HERMES, *Airapetian A., et al.*, JHEP **06**, 2008, 066, arXiv:0802.2499.

[14] *Belitsky A. V., Müller D., Kirchner A.*, Nucl. Phys. **B629**, 2002, 323, hep-ph/0112108.

[15] HERMES, *Airapetian A., et al.*, Phys. Lett. **B704**, 2011, 15, arXiv:1106.2990.

[16] *Belitsky A. V., Müller D.*, Phys. Rev. **D82**, 2010, 074010, arXiv:1005.5209.

[17] *Belitsky A. V., Müller D., Ji Y.*, Compton scattering: from deeply virtual to quasi-real, 2012, arXiv:1212.6674.

[18] HERMES, *Airapetian A., et al.*, JHEP **1210**, 2012, 042, arXiv:1206.5683.

[19] *Brasse F., et al.*, Nucl.Phys. **B110**, 1976, 413.

[20] HERMES, *Airapetian A., et al.*, JHEP **11**, 2009, 083, arXiv:0909.3587.

[21] HERMES, *Airapetian A., et al.*, JHEP **06**, 2010, 019, arXiv:1004.0177.

[22] HERMES, *Airapetian A., et al.*, JHEP **1207**, 2012, 032, arXiv:1203.6287.

[23] *Guidal, M.*, Eur. Phys. J. **A37**, 2008, 319, arXiv:0807.2355.

[24] *Guidal, M.*, Phys. Lett. **B689**, 2010, 156, arXiv:1003.0307.

[25] *Guidal, M.*, Phys. Lett. **B693**, 2010, 17, arXiv:1005.4922.

[26] *Kumerički K., Müller D., Schäfer A.*, JHEP **1107**, 2011, 073, arXiv:1106.2808.

[27] *Radyushkin A. V.*, Phys. Rev. **D56**, 1997 5524, hep-ph/9704207.

[28] *Goeke K., Polyakov M. V., Vanderhaeghen M.*, Prog. Part. Nucl. Phys. **47**, 2001, 401, hep-ph/0106012.

[29] *Vanderhaeghen M., Guichon P. A. M., Guidal M.*, Phys. Rev. Lett. **80**, 1998, 5064.

[30] *Freund A., McDermott M.*, Phys. Rev. **D65**, 2002, 074008, hep-ph/0106319.

[31] *Goloskokov S. V., Kroll P.*, Eur. Phys. J. **C42**, 2005, 281, hep-ph/0501242.

[32] *Goloskokov S. V., Kroll P.*, Eur. Phys. J. **C53**, 2008, 367, arXiv:0708.3569.

[33] *Freund A., McDermott M., Strikman, M.*, Phys. Rev. **D67**, 2003, 036001, hep-ph/0208160.

[34] *Goldstein G. R., Hernandez J.,Liuti S.*, Phys.Rev. **D84**, 2011, 034007, arXiv:1012.3776.

[35] *Diehl M., Ivanov D. Y.*, Eur. Phys. J. **C52**, 2007, 919, arXiv:0707.0351.

[36] *Kumerički K., Müller D., Passek-Kumerički K.*, Eur. Phys. J. **C58**, 2008 193, arXiv:0805.0152.

[37] *Kumerički K., Müller D., Passek-Kumerički K.*, Nucl. Phys. B **794**, 2008, 244, hep-ph/0703179.

[38] *Kumerički K., Müller D.*, Nucl. Phys. **B841**, 2010, 1, arXiv:0904.0458.

[39] *Müller D., Schäfer A.*, Nucl. Phys. **B739**, 2006, 1, hep-ph/0509204.

[40] *Shuvaev A. G.*, Phys. Rev. **D60**, 1999, 116005, hep-ph/9902318.

[41] *Polyakov M. V., Shuvaev A. G.*, "On 'dual' parametrizations of generalized parton distributions", 2002, hep-ph/0207153.

[42] *Kirch M., Manashov A., Schäfer A.*, Phys. Rev. **D72**, 2005, 114006, hep-ph/0509330.

[43] *Bechler C., Müller D.*, "Generic modelling of non-perturbative quantities and a description of hard exclusive π^+ electroproduction", 2009, arXiv:0906.2571.

[44] *James F., Roos M.*, Comput. Phys. Commun. **10**, 1975, 343.

[45] *Kirchner A., Müller, D.*, Eur. Phys. J. **C32**, 2003, 347, hep-ph/0302007.

[46] *Teryaev O. V.*, Analytic properties of hard exclusive amplitudes, 2005, hep-ph/0510031.

[47] *Polyakov M. V., Weiss C.*, Phys. Rev. **D60**, 1999, 114017, hep-ph/9902451.

[48] *Diehl M., Feldmann T., Jakob R., Kroll P.*, Eur. Phys. J. **C39**, 2005, 1, hep-ph/0408173.

[49] *Kroll P., Moutarde H., Sabatie F.*, From hard exclusive meson electroproduction to deeply virtual Compton scattering, 2012, arXiv:1210.6975.

[50] *Mankiewicz L., Piller G., Radyushkin A.*, Eur. Phys. J. **C 10**, 1999, 307, hep-ph/9812467.

[51] *Frankfurt L. L., Polyakov M. V., Strikman M., Vanderhaeghen M.*, Phys. Rev. Lett. **84**, 2000, 2589, hep-ph/9911381.

[52] Jefferson Lab Hall A, *Camacho C. M., et al.*, Phys. Rev. Lett. **97**, 2006, 262002, nucl-ex/0607029.

[53] CLAS, *Girod F. X., et al.*, Phys. Rev. Lett. **100**, 2008, 162002, arXiv:0711.4805.

[54] CLAS, *Chen S., et al.*, Phys. Rev. Lett. **97**, 2006, 072002, hep-ex/0605012.

[55] H1, *Aktas A., et al.*, Eur. Phys. J. **C44**, 2005, 1, hep-ex/0505061.

[56] H1, *Aaron F., et al.*, Phys.Lett. **B681**, 2009, 391, arXiv:0907.5289.

[57] ZEUS, *Chekanov S., et al.*, JHEP **05**, 2009, 108, arXiv:0812.2517.

[58] ZEUS, *Chekanov S., et al.*, Phys. Lett. **B573**, 2003, 46, hep-ex/0305028.

[59] HERMES, *Airapetian A., et al.*, Phys. Lett. **B659**, 2008, 486, 0707.0222 [hep-ex].

[60] *Anikin I. V., Pire B., Teryaev O. V.*, Phys. Rev. **D 62**, 2000, 071501, hep-ph/0003203.

[61] *Belitsky A. V., Müller D.*, Nucl. Phys. **B589**, 2000, 611, hep-ph/0007031.

[62] *Kivel N., Polyakov M. V.*, Nucl. Phys. **B600**, 2001, 334, hep-ph/0010150.

[63] *Braun V. M., Manashov A. N.*, Phys. Rev. Lett. **107**, 2011, 202001, arXiv:1108.2394; JHEP **01**, 2012, 085, arXiv:1111.6765;

[64] *Braun V., Manashov A., Pirnay B.*, Phys.Rev. **D86**, 2012, 014003, arXiv:1205.3332; "Finite-t and target mass corrections to deeply virtual Compton scattering", 2012, arXiv:1209.2559.